A Micro-Engineered Heart Tissue Model of Desmin-related Cardiomyopathy Caused by Mutant αB Crystalin

Yasaman Kargar Gaz Kooh[1], Bahareh Bahmani[2], Chen Zhao[3,4], Ganesh Malayath[2], Leah Hayem[5], Ghiska Ramahdita[6], Huanzhu Jiang[2], Javier Santiago Perez[7], Hsin Yi Chou[2], Yuxuan Huang[6], Xiucui Ma[3,4,8], Guy Genin[2,6], David Rawnsley[3,4], Abhinav Diwan[3,4,8,9,10,11], Nathaniel Huebsch[1,2,6]

[1] Institute of Materials Science and Engineering, Washington University in St. Louis, St. Louis, MO, USA;

[2] Department of Biomedical Engineering, Washington University in St. Louis, St. Louis, MO, USA;

[3] Cardiovascular Division and [4] Center for Cardiovascular Research, Washington University in St. Louis, St. Louis, MO, USA;

[5] Department of Biology, Washington University in St. Louis, St. Louis, MO, USA;

[6] Department of Mechanical Engineering and Material Science, Washington University in St. Louis, St. Louis, MO, USA;

[7] Roy Vagelos Medical Scientist Training Program, Washington University in St. Louis, St. Louis, MO, USA;

[8] Saint Louis Veterans Affairs Medical Center, St. Louis, MO, USA;

[9] Department of Neurology, Washington University in St. Louis, St. Louis, MO, USA;

[10] Department of Cell Biology and Physiology, Washington University in St. Louis, St. Louis, MO, USA;

[11] Department of Obstetrics and Gynecology, Washington University in St. Louis, St. Louis, MO, USA;

24 **Corresponding Author:** Nathaniel Huebsch, PhD.

25 Whitaker Hall 300E

26 1 Brookings Drive

27 Saint Louis, MO, 63130

28 nhuebsch@wustl.edu

29 **Disclosure:** N.H. reports consulting for Organos, Inc. (Moraga, CA), which did not affect the
30 current study. A.D. reports consulting for clinical trials with Clario (previously ERT/Biomedical
31 systems); and serving on the scientific advisory board for Dewpoint Therapeutics, which did not
32 affect the current study.

33 **Key words:** human iPSC, engineered micro-heart tissues, cardiomyopathy, chaperone proteins

Abstract

Protein quality control (PQC) is essential for maintaining sarcomere integrity in cardiomyocytes. α Crystallin B chain (CRYAB) R120G mutation disrupts CRYAB's chaperone activity, leading to aggregation of CRYAB and its client proteins (including Desmin), leading to Desmin-related cardiomyopathy (DRM). Prior experimental systems for modeling DRM linked to CRYAB require massive overexpression of CRYAB mutant isoforms, raising questions about translational relevance. Here, we establish the first model of CRYAB-linked DRM that uses genome-edited hiPSC together with isogenic controls, allowing us to study the impact of mutant CRYAB expressed at near endogenous levels. Within micro-engineered heart tissues (μHT), CRYAB-R120G mutant hiPSC derived cardiomyocytes recapitulated key DRM hallmarks, including Desmin and CRYAB aggregation, contractile dysfunction, and increased vulnerability to PQC pathway inhibition. CRYAB-R120G mutant μHT also exhibited dysfunctional calcium-contraction coupling, which exacerbated contractile deficits at higher pacing frequencies. JAK1 inhibition with Itacitinib partially restored contractile function at higher pacing frequencies, suggesting JAK1 inhibition as a viable therapeutic strategy. By preserving human-specific structural and functional features, our μHT platform enables mechanistic characterization of proteotoxic cardiomyopathies and offers a scalable system for targeted drug screening.

51 **Introduction**

52 Heart failure remains a leading cause of death worldwide (1). Inherited cardiomyopathies
53 contribute significantly to early onset heart failure (2). Desmin-related cardiomyopathy (DRM) is
54 a form of familial cardiomyopathy that affects approximately 1 in 2000 individuals (3). It is caused
55 by mutations in key cytoskeletal components such as Desmin (4, 5) or its chaperone α-Crystallin
56 B chain (CRYAB) (6, 7). Among DRM-linked CRYAB mutations, the missense R120G variant,
57 which is inherited in an autosomal dominant fashion, is especially pathogenic. This mutation
58 promotes toxic aggregation of both CRYAB and Desmin, leading to sarcomere disorganization,
59 proteotoxic stress, and impaired contractile function (6-8).

60 DRM pathology is a striking example of dysfunctional cardiomyocyte protein quality
61 control (PQC). As "sarcomeres are a machine that must repair themselves while in motion (9)",
62 cardiomyocytes depend on highly regulated PQC networks to degrade or repair proteins that
63 become misfolded through genetic mutations or mechanical/oxidative stress (9, 10). Chaperones
64 like CRYAB first attempt to refold these misfolded proteins. Those that cannot be refolded are
65 tagged with poly-ubiquitin chains and sent to the ubiquitin-proteasome system for degradation.
66 The autophagy-lysosome pathway provides a second backup, where ubiquitinated proteins and
67 damaged organelles are taken up by autophagosomes that fuse with lysosomes for final clearance.
68 Together, these complementary PQC pathways preserve cardiomyocyte proteostasis (9, 11-14).

69 Failure of PQC, linked to genetic mutations or chemical stress induced by drugs like
70 proteosome inhibitors used for chemotherapy, causes cardiomyopathy (15, 16). This
71 cardiomyopathy occurs because accumulation of cytosolic aggregates of misfolded proteins
72 overwhelms the cellular PQC machinery, preventing *in situ* repair of the sarcomeres; this leads to
73 contractile failure and eventually cell death (17, 18). Proteotoxicity of Desmin aggregates is a

74 hallmark of DRM (18). Desmin, a muscle-specific intermediate filament protein that anchors
75 sarcomeres to organelles such as mitochondria to maintain structural integrity and force
76 transmission, is especially dependent on PQC (19, 20). Beyond DRM linked to mutations and
77 chemotherapy, Desmin aggregation has been linked to cardiac ischemia (21), highlighting the
78 potential broad relevance of understanding the pathogenesis of DRM and developing treatments.

79 DRM is strongly linked to the dysfunction of CRYAB, a small heat shock protein that is
80 abundantly expressed in cardiac muscle and which acts as a molecular chaperone for sarcomere
81 proteins including Desmin, preventing misfolding and guiding these proteins to their final location
82 in the sarcomere (Desmin itself resides in the Z-disc (21, 22)). The R120G mutation in CRYAB is
83 especially toxic because it weakens both the protein's structural stability and its chaperone activity.
84 Computational (23) and experimental studies (24, 25) show that the R120G mutation breaks key
85 stabilizing salt bridges (R120-D109 and R107-D80), collapsing the central cavity of the α-
86 crystallin domain, to expose hydrophobic regions by disrupting the IPI/β4-β8 interaction. This
87 leaves unpaired negative charge that introduces an overall electrostatic imbalance. This altered
88 surface charge likely makes mutant CRYAB bind more tightly to Desmin, trapping Desmin into a
89 misfolded complex (18), and driving formation of large and insoluble oligomers consisting of both
90 Desmin and CRYAB. These aggregates, in turn, can sequester other client proteins, leading to
91 marked cellular dysfunction.

92 Despite the clinical relevance of genetically inherited DRM and closely related drug and
93 ischemia-induced DRM, mechanisms underlying DRM remain poorly understood, and medical
94 management remains limited to symptomatic therapies such as heart failure medications (e.g., β-
95 blockers, ACE inhibitors) and antiarrhythmics, as there are no disease-specific therapies targeting
96 the protein aggregation pathology (7). Previous studies investigating CRYAB mutations like

97 R120G have relied on mouse models with transgene-mediated overexpression of the mutant
98 isoforms of this protein (18, 26-28). This raises two important concerns: First, as CRYAB itself
99 tends to be found aggregated in DRM, and the requirement for massive overexpression (typically
100 6-fold increase in absolute CRYAB level is required to induce cardiomyopathy phenotypes in mice
101 (27)) raises concerns about physiological relevance given the potential for overexpression to
102 induce aggregation as an experimental artifact. Second, in addition to concerns involving
103 requirements for high absolute CRYAB expression levels, the reliance on murine systems raises
104 questions about translatability to human cardiomyocytes (29), particularly given reported
105 differences in basal and stress-induced expression of heat shock proteins, such as HSP70, between
106 humans and rodents (30).

107 Cell culture-based model systems using human iPSC-derived cardiomyocytes (hiPS-CMs)
108 offer a species-relevant platform for studying cardiomyopathy (29). However, hiPS-CM are often
109 structurally and functionally immature, which has limited their application for disease modeling
110 (31-35). To overcome these limitations, we developed a 3D micro-engineered heart tissue (μHT)
111 platform using hiPS-CMs derived either from iPSC engineered to harbor a homozygous knock-in
112 of the CRYAB-R120G mutation, or isogenic controls. This allowed us to study pathology
113 associated with CRYAB mutations at near-physiologic expression levels. To our knowledge, this
114 is the first iPSC model of this mutation with near physiologic protein expression and paired with
115 an isogenic control, allowing mechanistic studies.

116 Because Desmin expression was poor in our hiPS-CM in baseline, we first compared
117 maturation-inducing chemical treatments to culture within 3D engineered μHT as means of
118 inducing physiologic Desmin expression and localization (36, 37). Strikingly, only hiPS-CM
119 within the μHT exhibited robust expression, with appropriate physiological localization to the Z-

120 disc, of this key intermediate filament protein. As in prior murine models of DRM linked to
121 CRYAB-R120 overexpression (18, 28), the knock-in R120G mutation in CRYAB caused marked
122 contractile dysfunction in μHT. Studies with voltage dyes and the genetically encoded calcium
123 indicator RGECO1.2 revealed that this contractile dysfunction was linked to dysregulated calcium-
124 contraction coupling, which made contractility deficits especially pronounced at higher pacing
125 frequencies. Functional pathology associated with the CRYAB-R120G mutation was associated
126 with aggregation in CRYAB and its client, Desmin. This proteotoxic stress has been shown to
127 activate inflammatory signaling cascades, especially JAK/STAT (38). Thus, we evaluated the
128 JAK1-specific inhibitor, Itacitinib, as a candidate DRM therapy. This treatment partially rescued
129 the contractility deficits associated with the CRYAB-R120G mutant μHT. These findings establish
130 the first cell culture-based model of DRM with physiologically relevant CRYAB-R120G
131 expression, enabling further mechanistic investigation and drug screening of DRM in a human
132 context.

133 **Results**

134 **Development of a high-throughput hiPS-CM based platform to study pathology associated**
135 **with the CRYAB-R120G point mutation.** In postnatal cardiomyocytes, Desmin is abundantly
136 expressed and is primarily localized to desmosomes and Z-discs (39, 40). At baseline, we observed
137 vanishingly low levels of Desmin expression in hiPS-CM, with only about 1 in 100 cells
138 expressing this protein. This is consistent with prior reports that deficient expression and
139 mislocalization of Desmin make DRM especially challenging to model in immature hiPS-CMs
140 (35). We thus evaluated two strategies for enhancing Desmin expression in hiPS-CM: (1) culturing
141 cells in monolayer using a defined metabolic maturation media (MM) (41, 42), and (2) co-culturing

142 cells with primary cardiac fibroblasts and extracellular matrix (ECM) under mechanical
143 stimulation within 3D μHT (**Supplemental Video 1**).

144 We first assessed a MM that uses fatty acids and the PPAR-δ agonist GW0742 to promote
145 hiPS-CM structural maturation in 2D culture (42) (**Fig. S1 A, B**). Analysis of cardiomyocyte
146 morphology facilitated by Cellpose (43) (**Fig. S1 C**), an unbiased and AI-assisted segmentation
147 package, confirmed that MM-induced structural maturation (significant cellular elongation with
148 no significant cellular hypertrophy) when compared against standard media (SM; RPMI-1640
149 supplemented with 2% B27 supplement) (**Fig. S1 D-G**). This is consistent with structural
150 maturation previously observed for monolayers cultured in this same MM (42). However, even
151 with this structural maturation, the overall number of hiPS-CM expressing Desmin was still
152 vanishingly small (~1%) (**see below**).

153 Given the lack of Desmin expression in monolayer cultures, we transitioned to a tissue
154 engineering approach (44). We formed μHT by co-encapsulating 95% hiPS-CMs with 5% primary
155 human cardiac fibroblasts into a mixture of exogenous ECM proteins within micro-wells
156 containing PDMS pillars (**Fig. 1 A, B; Fig. S2**).

157 Strikingly, even without maturation-inducing chemicals such as fatty acids, within μHTs
158 formed against compliant PDMS posts (E = 200 kPa, bending stiffness of 0.13 N/m corresponding
159 to applied force of 6.5 μN at 50 μm deflection estimated from finite element simulations), hiPS-
160 CM exhibited robust Desmin expression (**Fig. 1 C)**. Consistent with our prior studies on Desmin
161 staining in positive control postnatal human heart sections (21), Desmin in hiPS-CM within μHT
162 was co-localized with α-actinin at Z-discs (**Fig. 1 C**). Interestingly, within μHTs formed against
163 stiff PDMS posts (E = 2000 kPa, estimated bending stiffness: 1.3N/m corresponding to applied

164 force of 65 μN at 50 μm deflection; **Fig, S3 B**), hiPS-CM showed even more robust Desmin
165 expression, and similar Z-disc localization (**Fig. 1 C**).

166 Whole-mount immunostaining followed by high-resolution image stitching of μHTs
167 labeled for α-actinin, Desmin and Hoechst allowed visualization of the entire tissue construct and
168 localization patterns of Desmin within a single field of view. In this context, Desmin expression
169 appeared broadly uniform throughout the tissue, with no obvious regional bias between the central
170 shaft and areas close to the PDMS posts (**Fig. 1 D** and **Fig. S4)**. These results suggest that Desmin
171 expression is independent of spatial proximity to mechanical anchor points.

172 To gain insights into whether culture in μHT caused a uniform, per-cardiomyocyte increase
173 in Desmin, or if Desmin expression was instead driven by an "elite" sub-population of cells, we
174 again turned to AI-assisted cell segmentation. Unambiguous, automated identification of cell
175 boundaries in the stained μHT, even with membrane-specific stains like wheat germ agglutinin
176 (WGA) proved challenging **(Fig. S5)**. Moreover, cortical staining for α-actinin, which was highly
177 prominent in 2D monolayers (**Fig. 1 C** and **Fig. S1 B)**, was not strongly apparent in 3D μHT,
178 making it difficult even for trained observers to identify individual cells (45). We thus developed
179 a custom image segmentation approach designed for dense tissue environments (**Supplement**
180 **Video 2, Fig. 1 E**). In this method, individual cell boundaries are estimated from nuclear staining
181 alone; the approach exploits the general observation that even in high density 3D tissues like μHT,
182 nuclei can typically be identified in an unbiased, unambiguous manner. Because of the high cell
183 density of μHT (**Fig. 1 C**), we assumed that each cell "grows out" from the nucleus to occupy
184 space until it impinges on the borders of its neighbors. Algorithmically, we accomplished this with
185 an approach inspired by traditional watershed segmentation and the growth of crystals from the
186 melt of crystalline phase materials (46). First, a circular border was applied to each identified

187 nucleus. Next, each border was allowed to expand until they impinged upon the expanding border
188 of its nearest neighbors (**Fig. 1 E)**. The estimated projected area and shape of each cell was then
189 quantified.

190 Morphological estimations suggested a significant increase in overall hiPS-CM area
191 within μHTs formed against stiff posts (**Fig. 1 F**), consistent with prior observations by our group
192 and others that hiPS-CM undergo hypertrophy when working against a higher afterload (47-49).
193 However, this analysis revealed no correlated changes in estimated eccentricity (**Fig. S6 A**),
194 elongation (**Fig. S6 B**), or circularity (**Fig. S6 C**).

195 Finally, we measured Desmin expression in each identified cell. Remarkably, this analysis
196 revealed that on average, ~30% of hiPS-CM in a given μHT region of interest expressed Desmin,
197 regardless of post rigidity (**Fig. 1 G**). While the percentage of Desmin-positive cells was similar
198 in μHT working against posts with different stiffness (**Fig. 1 G**), the percent of Desmin-positive
199 area in each identified cell was significantly higher in μHTs working against a higher afterload
200 (**Fig. 1 H**). This suggests that afterload is a key determinant of hiPS-CM Desmin expression. A
201 similar trend was observed in mutant CRYAB-R120G μHTs, which exhibited increased estimated
202 cell area (**Fig. S7 A**), but reduced elongation (**Fig. S7 B**), eccentricity (**Fig. S7 C**), and no change
203 in circularity (**Fig. S7 D**). As in the isogenic control, the percent of Desmin-positive cells was
204 comparable across conditions (**Fig. S7 E**); however, the percent of Desmin-positive area per cell
205 was significantly greater in μHTs working against stiffer posts (**Fig. S7 F**).

206 On a small scale, Desmin expression appeared to follow a distinct pattern: hiPS-CM
207 positive for Desmin were mostly found in clusters, close to one another, rather than being randomly
208 distributed throughout the tissue. To demonstrate this clustering pattern in a robust manner, we
209 performed computational simulations to ask how often, in a population where 30% of cells are

210 Desmin-positive, would we expect to find the Desmin positive cells in larger clusters (>2
211 cells/cluster) if the cells were distributed randomly (**Fig. S8**). This analysis confirmed our
212 observation that indeed, the Desmin positive hiPS-CM within μHT tend to group into large cluster
213 (**Fig. 1 I**).

214 Quantification of the Ripley's K-statistic, borrowed from geospatial analysis to formally
215 test the spatial relationship amongst objects (50), further validated the non-random, clustered
216 spatial distribution of Desmin-positive cardiomyocytes (**Fig. 1 I** and **Fig. S8 A, B**); with cluster
217 sized averaging ~ 30 μm radius (**Fig. S8 D-F**). These observations suggest the possibility that
218 localized paracrine signaling and/or localized changes in rigidity of the fibrous tissues are means
219 through which afterload enhances Desmin expression (51).

220 Overall, these results suggest that while metabolic maturation media can improve some
221 aspects of hiPS-CM structural maturation in 2D culture, it is not sufficient to induce Desmin
222 expression. In contrast, forming 3D μHT with mechanical loading leads to robust Desmin
223 expression.

224 **hiPS-CMs harboring the CRYAB-R120G point mutation exhibit Desmin aggregation.**
225 Having demonstrated an ability to assess Desmin structure within μHT, we next asked whether
226 human cardiac myocytes harboring the DRM-associated R120G mutation in CRYAB would
227 exhibit Desmin abnormalities without a requirement for massive overexpression of the mutant
228 protein. Using CRISPR/Cas9, we generated an isogenic hiPSC line homozygous for the CRYAB-
229 R120G mutation. Within μHT, hiPS-CMs harboring mutant CRYAB showed similar levels of
230 Desmin-positive cells (**Fig. 2 A** and **Fig. S9 A**) and Desmin-positive area (**Fig. 2 B**) compared to
231 hiPS-CM in isogenic control μHT. Strikingly, CRYAB mutant tissues showed significant
232 structural disorganization and aggregation of Desmin. Quantitatively, this was related to similar

233 number of Desmin-positive cells in aggregated form (**Fig S9 B**) but with a markedly increased
234 area of hiPS-CM expressing Desmin in an aggregated form rather than Z-disc-localized pattern
235 (**Fig. 2 C).** Moreover, consistent with reports that transgenic R120G mice develop cardiac
236 hypertrophy (28), DRM mutant tissues exhibited a statistically significant increase in estimated
237 cardiomyocyte size (**Fig. 2 D)**.

238 Mutations in CRYAB, including R120G, have been associated with disruptions of this
239 protein's chaperone functions, thereby leading to aggregation of client proteins like Desmin, but
240 also with aggregation of CRYAB itself (6). We thus examined CRYAB levels and localization
241 within the μHT. Strikingly, we observed that the mean CRYAB expression per cell was elevated
242 nearly 2-fold in hiPS-CM harboring the R120G mutation (**Fig. 2 E, F**). This may result from
243 inhibited clearance of aggregate-associated CRYAB-R120G, leading to an effective increase in
244 steady-state levels of this protein.

245 **CRYAB-R120G mutant μHTs exhibit contractile deficits.** Under low afterload conditions (soft
246 posts; **Fig. 3 A**), CRYAB-R120G μHTs showed significant deficits in contractile performance, as
247 illustrated by representative force traces highlighting disrupted force development and slower
248 contractile kinetics compared to isogenic controls (**Supplemental Video 3**; **Fig. 3 B**). This was
249 reflected in depressed peak active force (**Fig. 3 C**) and reduced contraction speed (**Fig. 3 D**).
250 Importantly, these deficits persisted under high afterload conditions (stiff posts; **Fig. 3 E**), where
251 CRYAB-R120G (**Supplemental Video 4**) μHTs again showed significantly reduced peak active
252 force and contraction speed (**Fig. 3 F-H**). Quantitative analysis of additional contraction
253 parameters, summarized in the heatmap (**Fig. 3 I, Fig. S10**), further supports the marked
254 hypocontractile phenotype in CRYAB mutant μHTs. Mutant μHTs showed slower contraction and

255 relaxation speeds, lower active stress, and lower peak deflections compared to isogenic control,
256 regardless the post stiffness.

257 Given that stiffer post conditions promoted greater hiPS-CM Desmin expression consistent
258 with prior findings that afterload enhances maturation of engineered heart tissues (47), along with
259 physiologic hypertrophy and more robust sarcomere organization (**Fig. 1**), and higher peak active
260 force compared to soft posts, we prioritized the high afterload (elastic modulus: 2000 kPa) posts
261 for subsequent analyses.

262 **CRYAB-R120G mutation make μHT more vulnerable to disruptions in protein quality**
263 **control pathways.** We next tested whether disrupting the heat shock protein system via the
264 CRYAB-R120G mutation would make μHT more vulnerable to inhibition of either of the two
265 alternative PQC pathways, the ubiquitin-proteasome system and lysosome-autophagy. To assess
266 vulnerability to ubiquitin-proteasome system inhibition, we treated μHTs with Bortezomib (100
267 nM) for 48 hours. Immunofluorescence analysis of Desmin and α-actinin following Bortezomib
268 exposure further supported this vulnerability. While both isogenic control and CRYAB-R120G
269 μHTs exhibited Desmin aggregation after proteasome inhibition **(Fig. 4 A)**, sarcomeric α-actinin
270 striation patterns remained relatively preserved in isogenic controls. In contrast, CRYAB-R120G
271 μHTs displayed extensive sarcomere disorganization, with poorly aligned myofibrils. Contractility
272 was measured in the same tissues before and after treatment, and the contractility index was
273 defined as the ratio of post-treatment to pre-treatment peak active force. Consistent with our
274 expectation, CRYAB-R120G μHTs showed a significantly greater reduction in contractile index
275 following Bortezomib exposure compared to isogenic controls **(Fig. 4 C).**

276 To evaluate whether the CRYAB-R120G mutant μHT were similarly vulnerable to
277 disruption of PQC through inhibition of autophagy-lysosome system or not, we treated μHTs with

278 10 nM Bafilomycin for 48 hours. As with inhibition of the ubiquitin-proteasome system, CRYAB
279 mutant μHT were more vulnerable than isogenic controls to inhibition of autophagy.
280 Immunostaining confirmed this vulnerability at the structural level (**Fig. 4 B**). Desmin aggregates
281 were present only in CRYAB-R120G μHTs following Bafilomycin treatment. Additionally,
282 sarcomeric α-actinin organization remained relatively preserved in isogenic controls, while
283 CRYAB-R120G μHTs showed clear disruption of sarcomeric striations. While isogenic control
284 μHTs maintained contractile performance with minimal change (contractile index ~1), CRYAB-
285 R120G μHTs showed a significant drop in force production following autophagy inhibition (**Fig.**
286 **4 D**). Altogether, these observations support the hypothesis that by weakening cardiomyocyte PQC
287 through inhibition of the heat shock protein response, mutations in CRYAB make these cells more
288 vulnerable to inhibition of the ubiquitin-proteasome system or of the lysosome-autophagy system
289 (52) and autophagy reactivation via TFEB (18) or ATG7 can restore proteostasis (53). Cytoskeletal
290 stress, whether mechanical, genetic, or proteotoxic, further accelerates PQC exhaustion,
291 decreasing contractile dysfunction (54, 55).

292 **Action potential waveform is grossly preserved in CRYAB-R120G μHTs.** Given the marked
293 deficits in contractile force and altered contractile kinetics of CRYAB-R120G mutant μHT, we
294 sought to determine potential alternations in electrophysiology and/or calcium handling that might
295 contribute to this pathology. We first labeled μHTs with the far-red voltage-sensitive dye BeRST-
296 1 and recorded optical action potentials using high-speed fluorescence imaging (**Fig. 5 A**).
297 Representative traces revealed that both CRYAB-WT and CRYAB-R120G μHTs exhibited
298 similar action potential waveform morphology, particularly with respect to repolarization kinetics
299 (**Fig. 5 B**). Quantitative analysis further showed no significant change in the upstroke velocity
300 which is quantified as normalized background-corrected amplitude of the BeRST signal ($\Delta F/F_0$)
301 over upstroke duration time between CRYAB-WT and CRYAB-R120G μHTs (**Fig. 5 C**).
302 However, there was no significant differences between genotypes in key repolarization metrics,
303 including action potential durations to 30%, 50%, 80%, and 90% repolarization (APD_{30}-APD_{90},
304 respectively; **Fig. 5 D, I**). Interestingly, although total action potential duration was unchanged
305 between genotypes (**Fig. 5 I**), the time from baseline to peak depolarization (e.g., upstroke
306 duration), was slightly faster in CRYAB-R120G μHTs with lower background-corrected
307 amplitude of the BeRST signal ($\Delta F/F_0$), leading to a similar upstroke velocity between mutant and
308 control tissues **(Fig. 5 I, Fig. S12)**. Preserved action potential upstroke velocity in our study is
309 consistent with prior electrophysiological profiling in CRYAB-R120G transgenic mice, which
310 reported intact action potential waveforms. While our findings do not directly assess ion channel
311 function, they align with previous evidence suggesting no alteration in $Na_v1.5$ function (56).

312 **CRYAB-R120G μHTs exhibit impaired calcium handling.** As action potential analysis
313 suggested that impaired depolarization was unlikely to contribute to the contractility deficits of
314 CRYAB-R120G mutant μHT, we next assessed potential dysfunction in calcium handling. To
315 assess calcium dynamics in CRYAB-R120G μHTs, we transduced purified hiPS-CM monolayers
316 with AAV6 vectors expressing the genetically encoded calcium indicator RGECO1.2 prior to
317 making the μHT (**Fig. 5 E**). CRYAB-R120G tissues exhibited significantly reduced background-
318 corrected RGECO signal intensity compared to isogenic controls (**Fig. 5 F**). Furthermore, mutant
319 μHT showed significant reduction in the upstroke velocity which is quantified as the normalized
320 background-corrected RGECO signal intensity ($\Delta F/F_0$) over upstroke duration time (**Fig. 5 G)**.
321 Calcium transient decay kinetics were significantly faster in CRYAB-R120G μHTs across all
322 measured thresholds (e.g. decay from peak intensity to 75%, 50%, and 30% of peak intensity),
323 when compared to isogenic controls (**Fig. 5 H, I, Fig. S13**). Moreover, higher calcium transient
324 upstroke duration was observed in mutant μHTs (**Fig. 5 I**). Importantly, the relative change in
325 $\Delta F/F_0$ was significantly higher than the change in calcium transient decay, suggesting that
326 accelerated calcium transient decay reflects overall depressed calcium intake rather than enhanced
327 calcium handling (**Fig. S13**).

328 Furthermore, reduced Ca^{2+} intake, quantified via lower values for background-corrected RGECO
329 signal ($\Delta F/F_0$), is consistent with the hypothesis that the CRYAB-R120G mutation diminishes
330 sarcoplasmic reticulum function, leading to impaired calcium-induced calcium release (57).
331 Depressed sarcoplasmic reticulum function would be expected to manifest in exaggerated
332 contractile deficits at higher pacing frequencies because of inhibited calcium cycling (57). We thus
333 assessed the force-frequency response of the μHT. Isogenic control tissues exhibited a largely flat
334 force-frequency response up to a pacing frequency of 3.5 Hz (**Fig. 5 J**). This is consistent with
335 prior reports of a moderate degree of physiological maturation of hiPS-CM in engineered heart
336 tissues (58, 59). However, CRYAB-R120G mutant μHT exhibited a markedly negative force-
337 frequency response (**Fig. 5 J)**, consistent with the hypothesis that depressed calcium transient
338 amplitude is linked to a dysfunctional sarcoplasmic reticulum in these cells. Altogether, these
339 findings suggest that calcium handling dysfunction plays a key role in the hypocontratile
340 phenotype of the CRYAB-R120G mutant μHT.

341 **Itacitinib treatment reduces STAT1 activation and partially rescues contractile deficits in**
342 **CRYAB-R120G μHTs.** In prior work, an unbiased screen performed in neonatal rat ventricular
343 cardiomyocytes identified JAK/STAT signaling in the generation of proteotoxic aggregates in the
344 setting of CRYAB-R120G overexpression (38). Subsequent investigation suggested that
345 JAK/STAT signaling via JAK1 inhibitors, including Itacitinib, could effectively remove such
346 aggregates (60, 61). We thus tested the potential of JAK1 inhibition via Itacitinib as a candidate
347 treatment for DRM. μHTs were exposed continuously to Itacitinib for one week (**Fig. 6 A**).
348 Following treatment, we fractionated the lysates of μHT to separately assess the soluble
349 (cytoplasmic) and insoluble (aggregate and cytoskeletal) fractions to assess STAT1 signaling (**Fig.**

350 **6 B)**, along with CRYAB expression and portioning into detergent-insoluble aggregates, by
351 Western blot.

352 In the soluble fraction (**Fig. 6 C)**, treatment with Itacitinib led to a dose-dependent
353 reduction in phosphorylated STAT1 (pY701) in both isogenic controls and CRYAB-R120G
354 tissues, confirming effective inhibition of JAK/STAT signaling. Total STAT1 levels were higher
355 in mutant μHTs, however, overall STAT1 levels remained unchanged with drug treatment. Soluble
356 CRYAB levels also appeared higher in mutant μHTs than isogenic controls, consistent with our
357 immunofluorescence data (**Fig. 2 E, F**).

358 In the insoluble lysate fraction, which includes aggregated, nuclear, and myofilament
359 proteins (**Fig. 6 D**), phosphorylated STAT1 was also decreased in a dose-dependent manner for
360 both isogenic controls and mutant μHTs. Total STAT1 levels also remained unchanged across
361 different treatment conditions. Moreover, CRYAB level was higher in the insoluble fraction of
362 CRYAB-R120G tissues regardless of treatment compared to isogenic controls (**Fig. 6 D)**.

363 To assess the functional consequences of JAK1 inhibition, contractile performance was
364 measured before and after treatment. Based on our finding that the force-frequency response is
365 especially impaired in DRM-μHT (**Fig. 5 J**), we assessed contractile performance both at 1 Hz and
366 2 Hz. Strikingly, in isogenic control (CRYAB-WT) μHT, Itacitinib treatment significantly
367 improved peak active force (**Fig. S14 A**) at both 0.1 μM and 1 μM doses under both pacing
368 conditions; with improved contractility index (ratio of peak active force before and after drug
369 exposure) at both frequencies (**Fig. 6 E-F**). In contrast, CRYAB-R120G μHTs demonstrated
370 recovery of contractility at 2 Hz following treatment with 0.1 μM Itacitinib without significant
371 improvement at 1 Hz (**Fig. S14 A)**. While absolute contractility at this pacing frequency did not

372 match isogenic control μHT treated with the same drug dose (0.1 μM), it was not significantly
373 different from isogenic control tissues treated with vehicle (**Fig. S14 A**).

374 0.1 μM Itacitinib also improved the relaxation velocity in both genotypes (**Fig. S15 A-C**).
375 However, even with this improvement, drug-treated CRYAB mutant μHT failed to match the
376 relaxation velocity of vehicle-treated isogenic controls (**Fig. S14 B**). These results suggest that
377 while JAK/STAT inhibition enhances contractile function in μHT, regardless of genotype, it
378 partially rescues contractility in the context of CRYAB-R120G induced proteotoxicity.
379 Interestingly, higher doses of Itacitinib did not further enhance contractility and instead appeared
380 to impair function, suggesting that JAK/STAT signaling may have dual role. Prior work on
381 engineered heart tissues has shown that sustained IFN-γ exposure drives STAT1 activation,
382 leading to loss of contractile force and sarcomere disarray; and these detrimental effects are
383 prevented by JAK inhibition (62). However, *in vivo* studies of pressure overload induced
384 hypertrophy have revealed a protective role of STAT1 when stabilized by the deubiquitinase
385 USP13. Specifically, USP13 enhances STAT1 deubiquitination and stability, promoting its
386 transcriptional activity, improving mitochondrial function, and attenuating TAC- and AngII-
387 induced hypertrophy (63). Thus, excessive STAT1 activation under inflammatory stress (e.g., IFN-
388 γ) is maladaptive, while basal STAT1 stabilization under biomechanical stress can be
389 cardioprotective. This dual role likely explains why higher-dose JAK/STAT inhibition in our
390 model compromises function, highlighting the delicate balance between pathological and adaptive
391 STAT1 signaling.

392 **Discussion**

393 PQC systems are essential for maintaining cardiac function by ensuring the integrity of
394 sarcomeric and cytoskeletal proteins (18, 64, 65). In this study, we developed, to our knowledge,

395 the first *in vitro* human model of DRM using hiPS-CMs harboring a homozygous CRYAB-R120G
396 knock-in mutation expressed at endogenous levels, which are subjected to physiologically relevant
397 mechanical loading. Unlike previous DRM models that relied on supraphysiological
398 overexpression of mutant CRYAB (27), our genome-edited platform preserves physiological
399 CRYAB-client protein expression balance, which enable a more accurate assessment of disease
400 mechanisms and potential underlying protein-protein interactions. This model recapitulates
401 hallmark DRM phenotypes, including Desmin aggregation, cellular hypertrophy, contractile
402 dysfunction, altered calcium handling, and heightened vulnerability to proteostasis disruption,
403 within human cardiomyocytes. We demonstrate that JAK/STAT pathway inhibition, previously
404 proposed as a candidate for DRM therapy (60, 61), led to modest improvements in contractile
405 function.

406 Our findings further support the role of CRYAB in modulating Desmin filament structure;
407 prior studies indicate this occurs through direct, phosphorylation-dependent CRYAB-Desmin
408 binding (66-68). In CRYAB-R120G μHTs, increased Desmin aggregation and sarcomeric
409 disorganization were observed, consistent with electron-dense aggregates in previous reports (6,
410 28, 69). In those prior studies, these aggregates, with CRYAB at the core and Desmin at the
411 periphery, displaced Desmin from Z-discs and intercalated discs into cytosolic inclusions, which
412 also contained α-actinin and ubiquitin (18, 21, 70), indicative of collapsed sarcomere structure.
413 Functionally, CRYAB-R120G μHTs showed reduced peak active force and slower contraction-
414 relaxation kinetics, paralleling prior evidence that proteotoxic sarcomeric protein aggregates
415 disrupts Z-disc alignment and force transmission, therefore driving contractile deficits in DRM
416 (28, 70, 71) . In addition, these prior studies report mitochondrial abnormalities, such as reduced

417 Complex I and IV activity, swelling, cristae loss, and impaired ATP production, which could also
418 inhibit contractility (70, 72, 73).

419 While prior studies have emphasized roles for direct sarcomeric and mitochondrial damage
420 in CRYAB-DRM associated contractile dysfunction (28, 70-73), our findings suggest a significant
421 defect in calcium handling in CRYAB-R120G mutant tissues (**Fig. 4**). This was supported not only
422 by direct analysis of Ca^{2+} handling, but also by a markedly negative force-frequency response in
423 the mutant tissues. Together, these findings implicate insufficient sarcoplasmic reticulum calcium
424 loading, reflecting impaired refilling due to RyR2, SERCA2, or PLN dysfunction (74). Prior
425 reports indicate that loss of chaperone function in CRYAB-R120G mutants can lead to
426 destabilization of SERCA2 (75), reducing the sarcoplasmic reserve of calcium (57). This effect
427 likely reflects chronic stress on the sarcoplasmic and endoplasmic reticulum, as aggregation of
428 misfolded CRYAB-R120G proteins exacerbates sarcoplasmic and/or endoplasmic reticulum stress
429 and impairs calcium-handling capacity (75, 76).

430 Therapeutically, JAK1 inhibition with Itacitinib partially restored contractile performance,
431 consistent with expectations based on prior work showing that CRYAB-R120G aggregation is
432 largely rescued by JAK1 inhibition (60, 61). Indeed, clinically approved JAK1 inhibitors enhance
433 ubiquitin-proteasome aggregate clearance via muscle-specific E3 ligases such as Asb2 (38, 77),
434 highlighting JAK1 as a promising target for DRM therapy. However, our finding that JAK1
435 inhibition only partially rescued contractility of the CRYAB-R120G μHT, with the effect more
436 pronounced at higher pacing frequency, and evidence suggesting that doses higher than 0.1 μM
437 appeared to have diminished physiological benefit, without a rescue of CRYAB-R120G portioning
438 into aggregates. This suggests the potential for a more multifaceted role for JAK/STAT signaling
439 in DRM suggesting that a complete shutdown of JAK/STAT signaling may be deleterious, whereas

440 finely tuned modulation is protective (78, 79). Prior studies highlight the dual nature of JAK/STAT
441 signaling. In ischemia–reperfusion models, excessive activation of JAK/STAT exacerbates injury,
442 whereas its inhibition reduces infarct size and apoptosis (80). Similarly, Pan *et al.* showed that
443 mechanical stretch rapidly activates JAK/STAT in cardiomyocytes via gp130 cytokines, linking
444 physiological stress to hypertrophic adaptation (81). Moreover, chronic or excessive pathway
445 activation has been consistently associated with maladaptive remodeling, hypertrophy, and fibrosis
446 (79). In contrast, consistent with the potential for JAK/STAT signaling to play a beneficial role in
447 cardiomyocytes, especially in the setting of mechanical stress, recent work suggests that loss of
448 STAT1 is deleterious in cardiac hypertrophy provoked by transaortic constriction *in vivo* (63),
449 highlighting the context-dependent nature of this pathway.

450 Our findings on the importance of JAK/STAT signaling in μHT, and a potential need for
451 basal, but not excessive, levels of these signals, also align with work in engineered human
452 myocardium. Zhan *et al.* reported that IFN-γ exposure, which strongly upregulates JAK1/STAT1,
453 caused sarcomeric protein loss and contractile decline, effects that were fully rescued by JAK
454 inhibitors (62). In contrast, Ho *et al.* reported that IFN-γ–induced STAT1 activation promoted
455 maturation of hESC-derived cardiomyocytes, enhancing calcium handling, sarcomere alignment,
456 and metabolic switching to fatty acid oxidation which were reversed by ruxolitinib (82, 83). Taken
457 together, these studies and our results suggest that modest JAK/STAT activity, is essential for
458 homeostasis, maturation, and stress adaptation. However, chronic overactivation or complete
459 pharmacological suppression can both impair cardiac function. The diminished rescue we
460 observed at higher Itacitinib doses may therefore reflect the loss of necessary adaptive pSTAT1.

461 Our finding that Desmin expression was preferentially induced in 3D μHT is consistent
462 with reports that 3D cardiac aggregates show higher Desmin expression than 2D cultures (84).
463 Like prior work from our team (48, 85) and others (86-88), this highlights that hiPS-CM change
464 their biology in physiologically relevant culture systems, which can facilitate disease modeling.
465 Desmin is the major muscle-specific intermediate filament protein in cardiac, skeletal, and smooth
466 muscle. It forms a 3D scaffold around Z-disks, linking myofibrils to the sarcolemma,
467 mitochondria, nuclei, and cell junctions. Although not essential for early development (as reflected
468 in our finding that Desmin is absent in immature cardiomyocytes) it becomes indispensable
469 postnatally for maintaining structural integrity and function (65).

470 The mechanical function of Desmin, coupled with the mechanical stresses that hiPS-CM
471 experience within μHT, suggest that mechanical stress is key to Desmin expression and/or
472 stability. Desmosomes are likely to be more prevalent in 3D, and Desmin intermediate filaments
473 directly interface with desmosomes to bear mechanical stress during coordinated contraction.
474 Recent work shows that desmosome–intermediate filament systems actively facilitate
475 mechanotransduction at adherens junctions by amplifying tension-sensitive RhoA signaling (89).
476 Moreover, Desmin has been shown to integrate 3D mechanical properties of muscle by coupling
477 transverse and longitudinal stress and contributing to load-dependent stiffness and viscoelasticity,
478 suggesting that its expression is sensitive to mechanical load (90). Thus, the induction of Desmin
479 expression in 3D μHT may represent an adaptive response to the stress-bearing and
480 mechanosignaling role of desmosomes, reinforced by ECM-mediated signaling, whereas in 2D
481 cultures, components of cell-cell junctions, including desmosomes, would be expected to
482 experience less mechanical loading, thereby requiring less reinforcement from Desmin
483 intermediate filaments for structural integrity (84, 91, 92).

484 In summary, our CRYAB-R120G μHT model recapitulates the complex interplay between
485 Desmin aggregation, PQC exhaustion, altered calcium handling, and inflammation. This positions
486 DRM as a prototypical model for studying PQC failure and sarcomere degeneration, with our
487 system offering a versatile platform for dissecting mechanisms and screening therapies in both
488 inherited and acquired cardiomyopathies.

489 Compared to prior experimental systems for modeling PQC-associated DRM, our model
490 has several advantages. First, previous DRM models using transgenic overexpression, which often
491 required excessive CRYAB levels (28), may have induced artificial protein-protein interactions
492 (93), whereas our model maintains endogenous gene expression dosage. Second, 3D μHT culture
493 promotes cardiomyocyte structural maturation, which includes Desmin expression, similar to
494 findings in previously described, more complex, macroscale engineered heart tissue models (35),
495 albeit with a requirement for ~20-fold fewer cells per construct, which offers advantages for
496 screening applications. Third, our data align with prior studies showing that Desmin functions as
497 a cytoskeletal scaffold critical for cardiomyocyte structural integrity (64, 65), and that its
498 organization is reinforced under mechanical loading in 3D systems similar to dyn-EHT (35).
499 Considering that chemotherapy agents such as doxorubicin and bortezomib disrupt PQC by
500 impairing proteasomal degradation and autophagic flux (94), our model of familial DRM may also
501 be useful in future studies to identify potential treatments for both genetic and drug-induced
502 cardiomyopathies involving proteotoxic stress.

503 Limitations of our μHT model include the short culture duration, and use of a homozygous
504 genotype rather than the more common heterozygous patient genotype (6). Future studies
505 incorporating single-cell omics, mitochondrial stress assessment, and heterozygous patient-

506 derived lines will likely enhance translational relevance, while live imaging of aggregation could
507 reveal dynamic mechanisms of disease progression.

508 **Methods**

509 **iPSC culture and differentiation**

510 Induced pluripotent stem cells with mKate-tagged α-actinin were previously described (95). These
511 cells were targeted with CRISPR-Cas9 at the Genome Editing and Stem Cell Center at Washington
512 University School of Medicine to generate homozygous knock in lines to change codon for
513 expression of arginine to glycine at position 120. We thank the Genome Engineering & Stem Cell
514 Center (GESC@MGI) at the Washington University in St. Louis for reagent validation services.
515 The mutation was validated by next generation sequencing and resulting R120G mutation in iPSC.
516 Isogenic controls (CRYAB-WT-iPSC) and mutant iPSC (CRYAB-R120G-iPSC) were cultured in
517 MTesR1 media (Fisher Scientific; NC1274780) and gradually adapted to StemFlex media (Life
518 Technologies; A3349401). During passaging and differentiation, iPSCs were passaged as single
519 cells using Gentle Dissociation Reagent (PBS with 1.8g/L NaCl and 0.5mM EDTA; (96), and
520 replated into media supplemented with 10 μM Y27632 (Biogem; 1293823) onto plates coated with
521 Geltrex (Life Technology; A1413302) at a concentration of 18.75 μg/cm^2. For differentiation,
522 iPSCs were subjected to timed control over Wnt signaling using small molecules (34, 48). Briefly,
523 iPSCs were seeded at a density of 40,000 cells/cm^2 onto Geltrex (37.5 μg/cm^2) and expanded for
524 3 days until confluent in MTeSR or StemFlex media. Next, media was changed to RPMI1640 (Life
525 Technologies; 11875093) supplemented with 150 μg/ml ascorbic acid (Fisher Scientific;
526 NC0602549) and 2% B27 without insulin (RPMI-I) (Life Technologies; A1895601) containing 6
527 μM CHIR99021 (Biogem; 2520691) (differentiation day 0). After 2 days, media was changed to
528 RPMI-I containing 5 μM IWP2 (Biogem; 6866167). After 2 additional days, media changed to

529 RPMI-I. On day 6, media was changed to RPMI1640 supplemented with 2% B27 (Life
530 Technologies; 17504044) (RPMI-C). Thereafter, culture was fed every 2 days with RPMI-C.
531 Beating cardiomyocytes were typically observed by differentiation day 8. On differentiation day
532 14, beating cardiomyocyte monolayer were gently dissociated using 10X TrypLE Select Enzyme
533 (Gibco; A1217701). The single cells were then replated onto Geltrex-coated tissue culture plastic
534 (37.5 μg/cm^2) at a density of 300,000 cells/cm^2 and cultured in RPMI-C media supplemented with
535 20% fetal bovine serum (FBS; Fisher Scientific; FB12999102) and 10 μM Y27632 for 24 hours.
536 At day 15, the media was changed to a lactate-based metabolic selection media (RPMI1640
537 without glucose (Millipore Sigma; R1383) supplemented with 4mM lactate (Fisher Scientific;
538 AAL1450014), 1% Non-Essential Amino Acids (Fisher Scientific; 11140050), and 1% Glutamax
539 (Fisher Scientific; 35050061)). On day 18, the media was replaced with fresh metabolic selection
540 media. After 6 days culture in metabolic selection media, from day 21 to 24, the media was
541 gradually changed back to RPMI-C for post-selection recovery. At differentiation days 24-26,
542 purified hiPS-cardiomyocytes (**Fig. S11 A**) were used for making μHT (**Fig. 1 A**).

543 **Monolayer Study**

544 Purified cells were dissociated and seeded onto Geltrex-coated Permanox chamber slides (Fisher
545 Scientific; 1256522) at density of 50,000 cells/cm^2. The replating media is RPMI-C with 10 μM
546 Y27632 and 10% FBS. For maturation media experiment, the media was changed to maturation
547 media (MM) consist of 125 μM palmitic acid (Fisher Scientific; NC1980206), 125 μM Linoleic
548 acid, 125 μM oleic acid (Millipore Sigma; L9655), and 5 μM GW0742 (MedChemExpress; HY-
549 13928) as PPAR-δ agonist in RPMI-without glucose supplemented with 2.8 mM Glucose, and 10
550 mM Galactose (41, 42). The media was changed to either fresh MM or fresh standard media (SM)
551 (RPMI-C) every 2 days for 2 weeks.

552 **Device Design**

553 The mold for the platform was designed in Autodesk Fusion 360 to fabricate 48 microwells, each
554 1.25 mm deep, containing two tapered posts 1 mm in height, with a 270 µm base diameter and a –
555 2° taper. The posts are capped to retain the tissues on their top, with the caps chamfered at 1° on
556 both the top and bottom edges while the central portion remains straight (total cap height: 250
557 µm). The distance between the two posts is kept as 1850 µm. The finalized designs were exported
558 as .stl files and uploaded to PreForm software for slicing, then printed on a Form 3 printer with a
559 50 µm layer thickness (**Fig. S2 A, B**).

560 **Device Fabrication**

561 Device fabrication was explained previously (44, 97). Briefly, PDMS microtugs were fabricated
562 using Hydrogel Assisted Stereolithographic Elastomer prototyping. After getting the master print
563 from Form 3 printer, devices were washed in dPBS and dried. To create the inverse-shape of the
564 microtugs, agar (Fisher Scientific; 1.5%wt/v in tap water) was boiled. Triton-X-100 was mixed to
565 a final concentration of 0.2% during the time it took for the agar to cool below the glass transition
566 temperature of the 3D prints. After reaching 60°C, the agar/Triton-X-100 mixture was poured onto
567 the 3D printed part, cooled down, and cross linked for 30 minutes at 4°C. Next, the 3D print was
568 gently removed from the agar, leaving the agar mold as an inverse shape. Sylgard 184 mixture was
569 prepared by mixing the crosslinker and base with 1:10 ratio and degassed under vacuum chamber.
570 In parallel, Sylgard 527 mixture was prepared by mixing part A and part B with 1:1 ratio, then
571 degassed in the same way. Afterwards, to make the stiff posts with elastic modulus of 2000 kPa
572 and theoretical bending stiffness of 1.3 N/m, pure Sylgard 184 was poured into the agar mold. In
573 parallel to make soft posts, Sylgard 184 mixture was mixed with Sylgard 527 mixture with 1:4
574 ratio, to yield PDMS with elastic modulus of 200 kPa and theoretical bending stiffness of 0.13

575 N/m. After pouring the PDMS mixture into the agar mold, it was degassed and kept at 37°C oven
576 overnight. The next day, PDMS devices were removed from agar and underwent final crosslinking
577 at 60°C overnight.
578 In the meantime, we fabricated polycarbonate inserts to contain the PDMS devices. Polycarbonate
579 inserts were created by thermoforming against a tooling mold 3D-printed in high-temperature resin
580 on a Phrozen Digital Light Printing (DLP) 3D printer as described previously (98). After forming
581 the polycarbonate inserts, PDMS microtug devices were attached to the inserts using Sylgard 184
582 as a glue, and the devices were then autoclaved and stored under aseptic conditions until ready for
583 cell seeding to form μHT.
584 **Surface modification**
585 To reduce the cell attachment to the sterilized PDMS devices, we submerged the devices in 1%
586 wt/v Pluronic F127 for at least 2 hours at room temperature, followed by 3 washes (five minutes
587 each) in sterile dPBS.
588 **iPSC-μHT formation and optimization**
589 Purified cardiomyocytes were gently dissociated using 10X TrypLE Select Enzyme (for up to 15
590 minutes). In parallel, human primary ventricular cardiac fibroblast (Lonza; CC-2904) were
591 dissociated using 0.25% trypsin EDTA (Fisher Scientific; 25200072) for 5 minutes. A mixture of
592 5% primary cardiac fibroblast and 95% of iPS-CMs, at a total cell density of 2×10^7 cells/ml were
593 encapsulated into 1.5 mg/ml collagen I rat tail (Fisher Scientific; A1048301) and 10% v/v Geltrex.
594 4 μL of this mixture (80,000 cells) was seeded into each 2-post μHT-forming device (**Fig. S2 C**).
595 The seeded devices were next incubated at 37°C with 5% CO2 for 20 minutes to crosslink
596 collagen, before the entire culture well was filled with μHT culture media (Knock out DMEM
597 (Life Technologies; 10829018) supplemented with 20% FBS, 1% Glutamax, 1% Non-essential

598 Amino Acids, 1% Pen Strep (Fisher Scientific; 15-140-122), 150 μg/ml ascorbic acid and 10 μM
599 Y27632). Tissue compaction was typically observed within 48 hours (**Fig. S2 C, D**).

600 **Immunostaining**

601 μHTs and monolayers were incubated in 100 mM KCl until cessation of spontaneous beating, and
602 then step fixed with 1%, 2%, 3% and 4% paraformaldehyde at 4°C, with each fixation step at least
603 1 hour, and washed in dPBS. These tissues were subsequently used for immunostaining for
604 sarcomeric α-actinin (Millipore Sigma; A7811), Desmin (Cell Signaling; 5332), and CRYAB
605 (Enzo Life Science; ADI-SPA-223). Wheat germ agglutinin (WGA) (Fisher; W11261) was used
606 for staining cell membranes, and cell nuclei were stained with Hoechst 33342. Whole mount tissue
607 or monolayer stained were mounted in ProLong Gold (99) (Fisher Scientific; P36930) and scanned
608 using a Fluoview FB1200 confocal microscope (Olympus, Tokyo, Japan). In-house structural
609 analysis codes are available here: (https://github.com/huebschlab/CardioSpatialAnalysis)

610 **AAV6-driven-ChR2(H134R) and/or RGECO1.2 constructs and transduction**

611 pAAV-CMV-CHR2-eYFP was from Vectorbuilder (VB240118-1580mnz). pAAV-CMV
612 backbone was generously provided by Dr. Brent French at University of Virginia, Charlottesville,
613 VA. CMV-R-GECO1.2 was a gift from Robert Campbell (Addgene plasmid #45494;
614 http://n2t.net/addgene:45494; RRID:Addgene_45494; (100)).

615 To generate pAAV-CMV-ChR2(H134R)-eYFP-P2A-RGECO1.2 construct, fragments encoding
616 ChR2(H134R)-eYFP and p2a-RGECO1.2 were PCR-amplified, restriction-digested, and ligated
617 into the pAAV-CMV backbone using T4 DNA ligase. Adeno-associated virus serotype 6 (AAV6)
618 particles coding for ChR2(H134R)-eYFP or ChR2(H134R)-eYFP-p2a-RGECO1.2 driven by
619 CMV promoter were generated by the Hope Center viral vectors core.

620 For AAV transduction, hiPS-CM monolayers were transduced following metabolic purification at
621 day 25 (MOI: 5×10^3, yielding ~100% transduction efficiency). Cells were exposed for 6 hours
622 in infection media (RPMI-C, 2% FBS, 1% Glutamax, 0.1% penicillin-streptomycin, 1% HEPES),
623 then recovered in culture medium (RPMI-C, 10% FBS, 1% Glutamax, 0.1% penicillin-
624 streptomycin, 1% HEPES) prior to μHT formation. Resulting μHT robustly expressed the vector,
625 exhibited RGECO1.2 based Ca^{2+} transient, and could be optogenetically paced by blue light for >
626 30 days.

627 **High-speed epifluorescence imaging**

628 Physiology of iPSC-μHT at tissue day 10 (corresponding to day 35 of hiPS-cardiomyocytes
629 differentiation) was analyzed using a high-speed imaging system (Eclipse Ts2R, Nikon; Tokyo,
630 Japan) equipped with a digital CMOS camera (Hamamatsu ORCA-Flash4.0 V2; Japan). The
631 imaging stage was set to a constant 37°C temperature using a thermal plate (Tokai Hit; Shizuoka,
632 Japan). Field pacing of tissue (1 Hz, 20 msec bipolar pulses, <20V) during imaging was achieved
633 using graphite electrodes (MyoPacer, Ion Optix, USA). 1 Hz field pacing was chosen because it is
634 slightly above the average spontaneous beating rate of the cardiac tissues. In parallel, instead of
635 field pacing with graphite electrodes, we used AAV6-ChR2 at MOI of 5,000 to pace the tissues
636 using GFP blue light. We also used AAV6-ChR2-RGECO1.2 to measure the calcium dynamic
637 with Texas red light.

638 **Contractility characterization**

639 Open source Beat Profiler software (101) was used to quantify tissue contractility. As an input to
640 this software, the theoretical bending stiffness of our μHT posts were determined by finite element
641 model using Ansys software. For soft posts (elastic modulus = 200 kPa), the bending stiffness was
642 0.13 N/m, corresponding to a 6.5 μN force required for 50 μm deflection. For stiff posts (elastic

643 modulus = 2000 kPa), the bending stiffness was 1.3 N/m, corresponding to a 65 μN force for 50
644 μm deflection.

645 **Action potential and calcium measurements**

646 Membrane potential was measured by labeling tissue with 1 μM BeRST-1 voltage sensitive dye
647 for 5 hours in phenol red free RPMI-C. Action potential waveforms were captured by imaging in
648 the Cy5 channel. Calcium transients were captured by imaging RGECO1.2 in the Texas red
649 channel. BeRST-1 and RGECO1.2 videos were analyzed via custom, open-source MATLAB code
650 (available at: https://huebschlab.wustl.edu/resources-2/; (102)); intensity profile and kinetics
651 parameters were automatically extracted. For calcium transient dynamics, initial baseline to peak
652 of the intensity was measured as UPD, times from the peak to 30, 50 and 75% decay of intensity
653 was characterized as decay30, decay50, and decay70. For action potential waveforms, initial
654 baseline to peak intensity was measured as UPD, and the time from action potential initiation to
655 30% decay from peak intensity (APD_{30}), along with the time from action potential initiation to
656 80% or 90% decay from peak intensity (APD_{80} and APD_{90}, respectively), were measured.

657 **Pharmacology studies**

658 The effect of sarcomeric PQC pathways for pathologic contractility in CRYAB-R120G induced
659 cardiomyopathy was investigated using pharmacological probes. Bortezomib was chosen as
660 ubiquitin-proteasome inhibitor (100 nM), and Bafilomycin (10 nM) as lysosome-autophagy
661 inhibitor. Drugs were first diluted in dimethyl sulfoxide (DMSO), then serial diluted in tissue
662 culture media with supplements. Before exposure to drug the tissues were imaged for contractility
663 measurement, then these drugs were used for 48 hours to evaluate the chronic exposure for protein
664 turnover incubation at 37°C with 5% CO_2 then imaged for contractility again. Finally, we

665 calculated the contractility index as the ratio of the peak active force after exposing to drugs over
666 before exposing to drug followed by fixation and immunostaining.
667 To study the potential impact of JAK/STAT inhibition as a therapy for DRM, we treated μHTs
668 with 0.1 μM and 1 μM Itacitinib, a JAK1 inhibitor, for 1 week to assess the role of inflammatory
669 signaling pathways, specifically examining pSTAT1 (Tyr701) and STAT1 levels, fresh drug was
670 added every day.

671 **Immunoblotting**

672 Soluble and insoluble protein fractions were isolated from μHTs by sequential extraction. Tissues
673 were first lysed in RIPA buffer (Cell Signaling; 9806) supplemented with 1% NP-40 to extract the
674 soluble protein fraction, collected as the supernatant following centrifugation. The remaining pellet
675 was then solubilized in 9 M urea to obtain the insoluble protein fraction. Immunoblotting was
676 performed as previously described (18). Specific antibodies are as follows: CRYAB (Enzo Life
677 Science; ADI-SPA-223), pSTAT1(Tyr701; Cell Signaling; 58D6), STAT1 (Thermo Fisher;
678 AHO0832), GAPDH (Abcam; ab22555), and Histone 3 (Cell Signaling; 9715).

679 **Quantification and statistical analysis**

680 GraphPad 9.3.1 was used for statistics and data visualization. Data are presented with mean ±
681 standard deviation (*SD*), and are pooled from μHT (or 2D monolayers) from at least 3 independent
682 differentiation batches. For quantitative analysis, data were first assessed for normality using
683 Normality and Lognormality tests. If datasets were normally distributed, comparisons between
684 two groups were performed using a parametric Student's t-test, and comparisons among multiple
685 groups were analyzed using parametric one-way ANOVA followed by Holm–Šidák post hoc test
686 for multiple comparisons. If datasets were not normally distributed, a non-parametric Mann–
687 Whitney U test was used for two-group comparisons, and one-way ANOVA with Dunn's

correction was applied for multiple group comparisons. When two independent variables were compared, data were analyzed using two-way ANOVA followed by Holm–Šidák post hoc test. All statistical analyses were performed as two-tailed tests unless otherwise specified.

Sources of funding:

A.D. was supported by grants from the National Institutes of Health (HL107594) and the Department of Veterans Affairs (I01BX005065, I01BX005981). D.R.R. is supported from grants from the National Institutes of Health (T32 HL007081 and 1K08HL163469). NH was supported by grants from National Institutes of Health (HL159094) and National Science Foundation CAREER (2338931). G.R. and H.Y.C were supported by McDonnell Academy Fellowship. J.S.P. was supported by T32GM007200

Figure 1

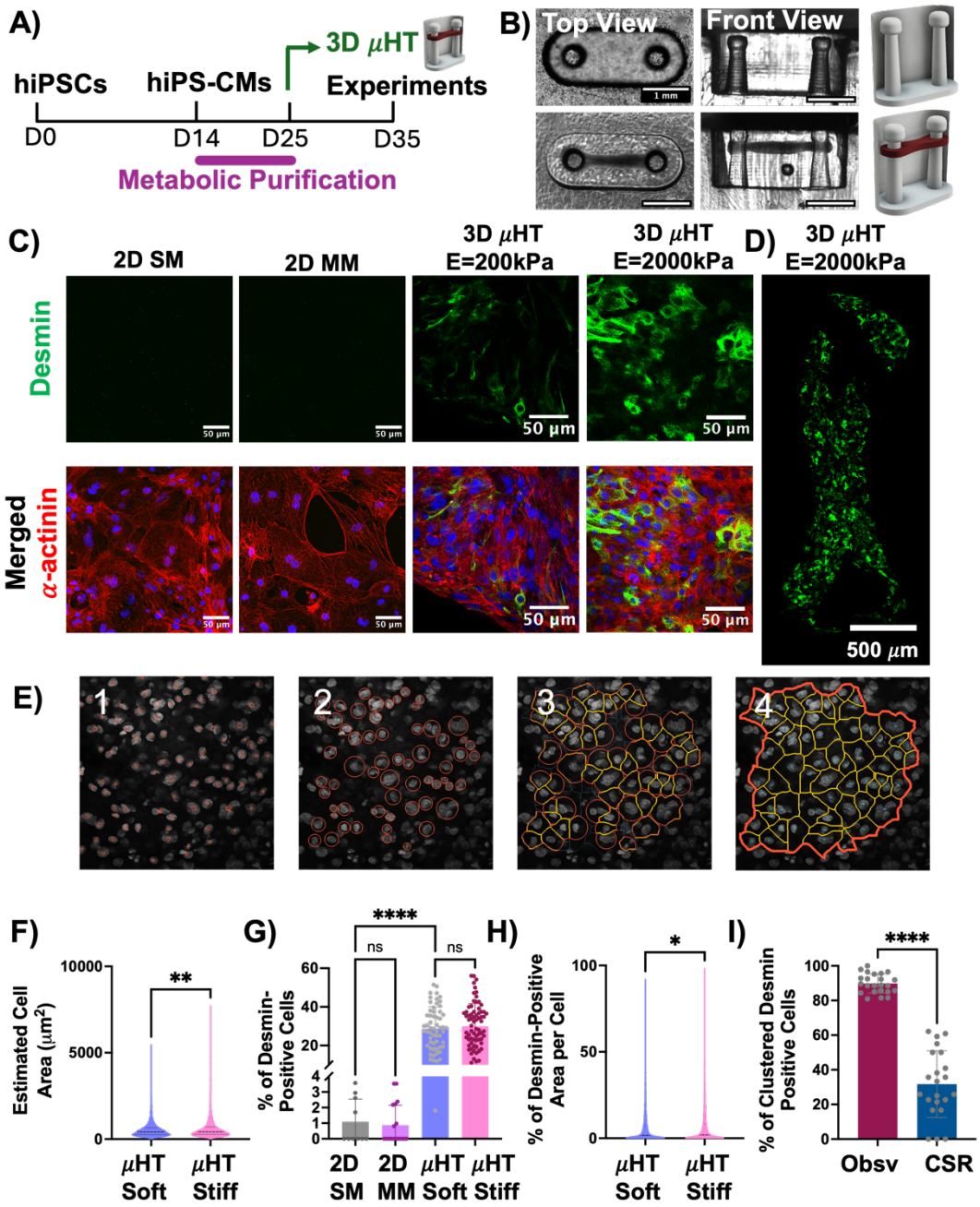

698

699 **Figure 1. Culture within 3D μHT triggers Desmin expression in hiPS-CM. (A)** Schematic of

700 the experimental timeline for generating 3D μHT from hiPS-CMs. Cells were differentiated from

701 hiPSCs (D0–D14), purified by metabolic selection (D14–D25), and seeded into 3D μHT devices

702 for culture from D25–D35 before analysis. **(B)** Representative brightfield images of μHTs from

703 top and front views on PDMS posts, alongside schematic micrograph of the post geometry with
704 and without tissue load. Scale bars: 1mm. **(C)** Immunofluorescence staining for α-actinin (red),
705 Desmin (green), and Hoechst (blue) in either 2D with SM or MM and μHTs cultured on soft (E =
706 200 kPa) or stiff (E = 2000 kPa) posts. Scale bars: 50 μm. **(D)** Wide-field view of the whole-mount
707 immunostaining for Desmin in 3D μHTs cultured on stiff posts. Scale bar: 500 μm. **(E)**
708 Representative images showing crystal growth from nuclear segmentation for cell shape analysis:
709 raw Hoechst stain (1), nuclei with red outlines (2), enlarging the cell boundary (3), and overlaid
710 segmentation boundaries (4). **(F)** Quantification of estimated cell area from nuclei-stained μHTs,
711 showing significantly increased cell area on stiff posts compared to soft posts; Data are presented
712 as mean ± *SD*; n values represent individual cells pooled from 3 independent differentiation
713 batches; *P* values by unpaired Student t-test, non-parametric, Mann-Whitney test; ** $p < 0.01$. **(G)**
714 Quantification of the percentage of Desmin-positive cells comparing 2D cultured in either SM or
715 MM with 3D μHTs within soft and stiff posts; Data are presented as mean ± *SD*; n values represent
716 individual 2D monolayers or individual μHTs pooled from 3 independent differentiation batches;
717 *P* values by one-way ANOVA, non-parametric, Kruskal Wallis test; **** $p < 0.0001$, ns = not
718 significant. **(H)** Quantification of the percentage of Desmin-positive area per cell in 3D μHTs,
719 revealing a significant increase in Desmin-positive area per cell on stiff posts. Data are presented
720 as mean ± *SD*; n values represent individual cells pooled from 3 independent differentiation
721 batches. *P* values by unpaired t-test, non-parametric, Mann-Whitney test; * $p < 0.05$. **(I)**
722 Quantification of the percentage of clustered Desmin-positive cells in 3D μHTs compared to
723 simulations of complete spatial randomness (CSR). Observed (Obsv) distributions showed
724 significantly higher clustering than CSR, supporting a non-random, localized expression of
725 Desmin-positive hiPS-CMs. Data are presented as mean ± *SD*; n values represent individual μHTs

726 pooled from 3 independent differentiation batches. *P* values by unpaired Student t-test, parametric

727 **** $p < 0.0001$.

Figure 2

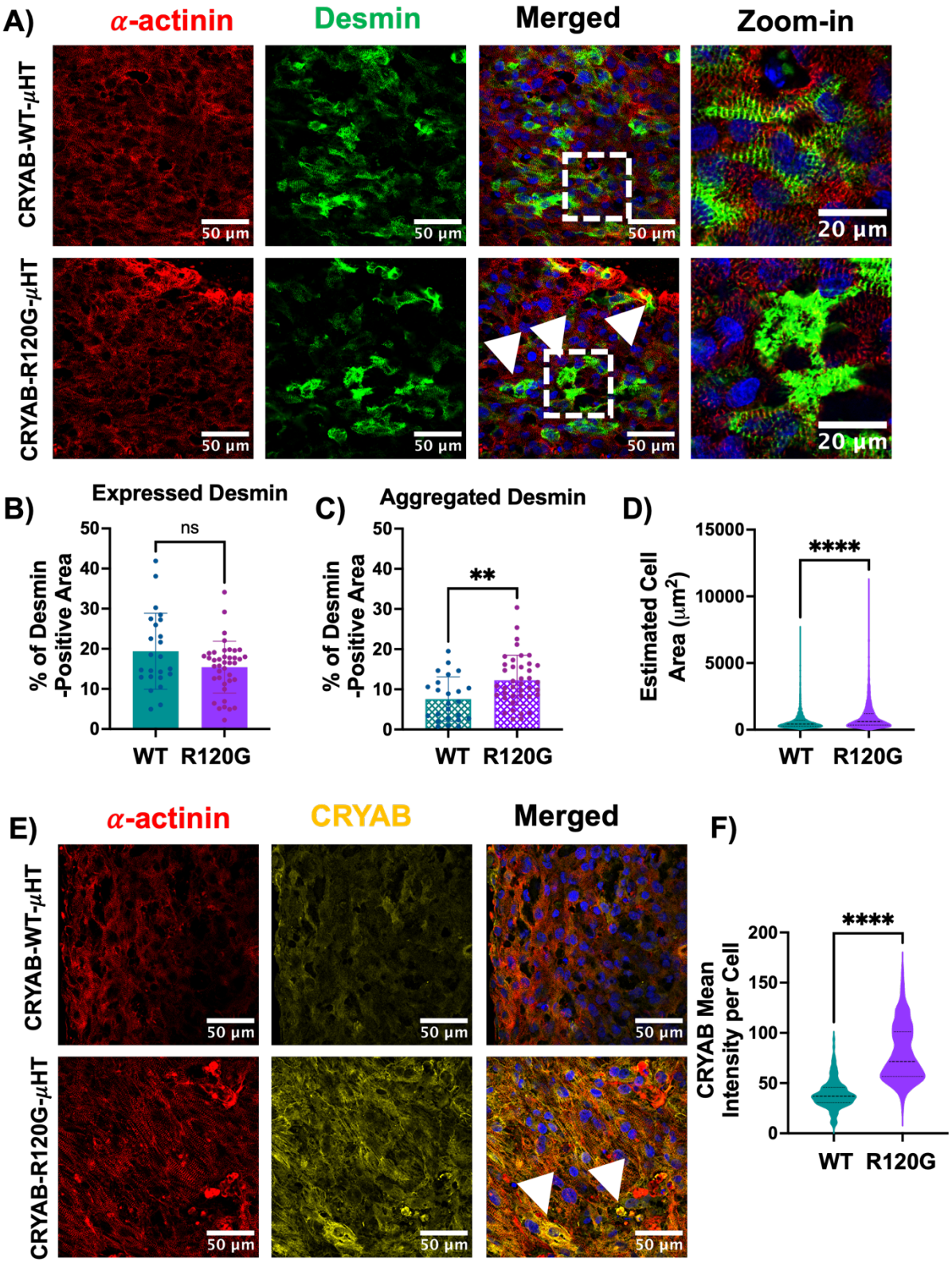
A)
α-actinin
Desmin
Merged
Zoom-in
CRYAB-WT-μHT
CRYAB-R120G-μHT
50 μm
20 μm
B)
Expressed Desmin
ns
% of Desmin -Positive Area
WT
R120G
C)
Aggregated Desmin
**
D)
Estimated Cell Area (μm²)
****
E)
CRYAB
F)
CRYAB Mean Intensity per Cell

728

729 **Figure 2. CRYAB-R120G mutation promotes Desmin aggregation and increases CRYAB**
730 **accumulation in 3D μHT. (A)** Immunofluorescence staining for α-actinin (red), Desmin (green),
731 and Hoechst (blue) in CRYAB-WT-μHT and CRYAB-R120G-μHT at day 35. Arrows indicate
732 regions of Desmin aggregation in CRYAB-R120G-μHTs. Scale bars: 50 μm (merged images), 20
733 μm (zoom-in). **(B, C)** Quantification of Desmin expression and aggregation in μHTs. **(B)** The
734 percentage of total tissue area occupied by Desmin-positive staining was measured across μHTs.
735 No significant difference was observed between WT and CRYAB-R120G μHTs. **(C)** The
736 percentage of Desmin-positive area in aggregation form was calculated relative to the total
737 Desmin-positive area. CRYAB-R120G μHTs showed a significantly higher proportion of
738 aggregated Desmin compared to WT. Data are presented as mean ± *SD*; n values represent
739 individual μHT pooled from 3 independent differentiation batches. *P* values were determined by
740 unpaired Student's t-test, parametric; ** $p < 0.01$. **(D)** Quantification of estimated cell area from
741 nuclei-stained μHTs demonstrate significantly higher estimated cell area in CRYAB-R120G
742 mutant μHTs compared to isogenic controls, consistent with a hypertrophic phenotype in this
743 mutation. Data are presented as mean ± *SD*; n values represent individual cells pooled from 3
744 independent differentiation batches. *P* values were determined by unpaired Student's t-test, non-
745 parametric, Mann–Whitney test; **** $p < 0.0001$. **(E)** Immunofluorescence staining for α-actinin
746 (red), CRYAB (yellow), and Hoechst (blue) in CRYAB-WT-μHT and CRYAB-R120G-μHT.
747 Arrow indicates region of CRYAB accumulation in CRYAB-R120G-μHTs. Scale bars: 50 μm.
748 **(F)** Quantification of mean CRYAB fluorescence intensity per cell, showing a significant increase
749 in CRYAB levels in CRYAB-R120G-μHTs compared to WT. Data are presented as mean ± *SD*;
750 n values represent individual cells pooled from ≥3 independent differentiations. *P* values by
751 unpaired t-test, non-parametric, Mann-Whitney test; **** $p < 0.0001$.

Figure 3

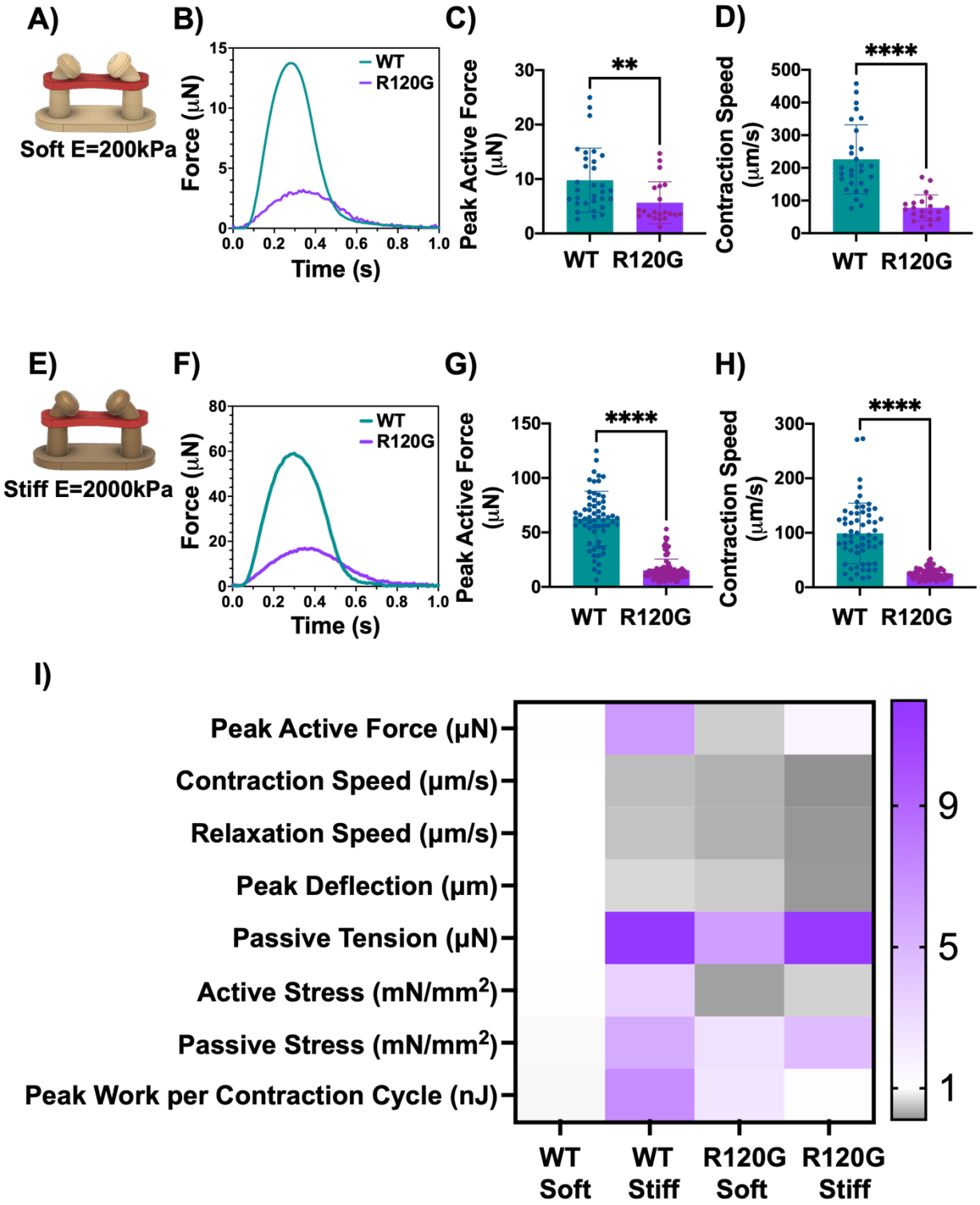

752

753 **Figure 3. CRYAB-R120G mutation reduces contractile performance of 3D μHTs. (A-D)** Soft

754 post condition (E = 200 kPa). **(A)** Schematic of 3D μHT on soft PDMS posts. **(B)** Representative

755 force–time traces for CRYAB-WT and CRYAB-R120G μHTs. Quantification of **(C)** peak active
756 force and **(D)** contraction speed, showing significantly impaired contractility in CRYAB-R120G
757 μHTs compared to WT. Data are presented as mean ± *SD*; n values represent individual μHT
758 pooled from ≥3 independent differentiations. *P* values by unpaired t-test, non-parametric, Mann-
759 Whitney test; **** $p < 0.0001$, ** $p < 0.01$. **(E-H)** Stiff post condition (E = 2000
760 kPa). **(E)** Schematic of 3D μHT on stiff PDMS posts. **(F)** Representative force–time traces for
761 CRYAB-WT and CRYAB-R120G μHTs. Quantification of **(G)** peak active force and **(H)**
762 contraction speed, showing a pronounced contractility deficit in CRYAB-R120G μHTs similar to
763 μHT cultured within soft posts. Data are presented as mean ± *SD*; n values represent individual
764 μHT pooled from ≥3 independent differentiations. *P* values by unpaired t-test, non-parametric,
765 Mann-Whitney test; **** $p < 0.0001$. **(I)** Heatmap of contractile and mechanical parameters across
766 conditions, including peak active force, contraction speed, relaxation speed, peak deflection,
767 passive tension, active and passive stress, and peak work per contraction cycle. All values were
768 normalized to the mean value of the WT soft condition, with darker purple indicating higher
769 normalized values.

Figure 4

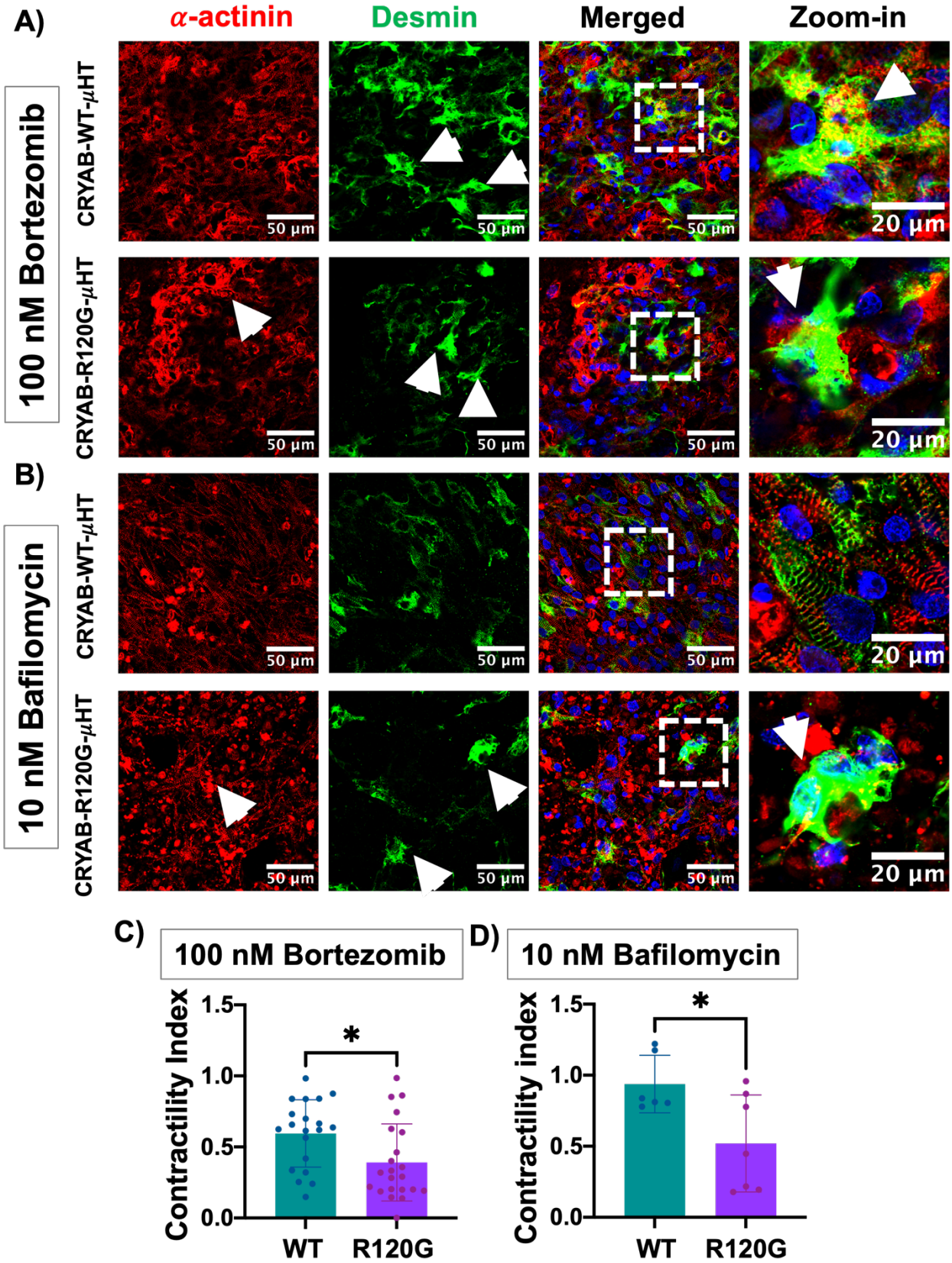
A)
α-actinin
Desmin
Merged
Zoom-in
100 nM Bortezomib
CRYAB-WT-μHT
CRYAB-R120G-μHT
50 μm
20 μm
B)
10 nM Bafilomycin
CRYAB-WT-μHT
CRYAB-R120G-μHT
C)
100 nM Bortezomib
Contractility Index
1.5
1.0
0.5
0.0
*
WT
R120G
D)
10 nM Bafilomycin
Contractility index
1.5
1.0
0.5
0.0
*
WT
R120G

770

771 **Figure 4. The CRYAB-R120G mutation increases vulnerability of μHT to ubiquitin-**
772 **proteasome and lysosome-autophagy inhibitors. (A)** Immunofluorescence staining for α-actinin
773 (red), Desmin (green), and Hoechst (blue) in CRYAB-WT-μHT and CRYAB-R120G-μHT treated
774 with 100 nM bortezomib for 48 hours. Arrows indicate regions of sarcomeric disruption and
775 Desmin aggregation. Zoom-in panels show that bortezomib treatment induces Desmin aggregation
776 in both WT and CRYAB-R120G μHTs, with additional sarcomeric disorganization in CRYAB-
777 R120G tissues. Scale bars: 50 μm (merged images), 20 μm (zoom-in). **(B)** Immunofluorescence
778 staining for α-actinin (red), Desmin (green), and Hoechst (blue) in CRYAB-WT-μHT and
779 CRYAB-R120G-μHT treated with 10 nM bafilomycin for 48 hours. Zoom-in panels show that
780 bafilomycin treatment induces Desmin aggregation in CRYAB-R120G μHTs but not in CRYAB-
781 WT μHTs, with preserved sarcomeric structure in isogenic controls. Scale bars: 50 μm (merged
782 images), 20 μm (zoom-in). Contractility index in CRYAB-WT and CRYAB-R120G μHTs treated
783 with **(C)** bortezomib or **(D)** bafilomycin (ratio of peak active force post-/pre-treatment). Both
784 treatments significantly reduced contractility in CRYAB-R120G μHTs compared to WT. Data are
785 presented as mean ± *SD*; n values represent individual μHTs pooled from ≥2 independent
786 differentiations. *P* values by unpaired t-test, parametric; * $p < 0.05$.

Figure 5

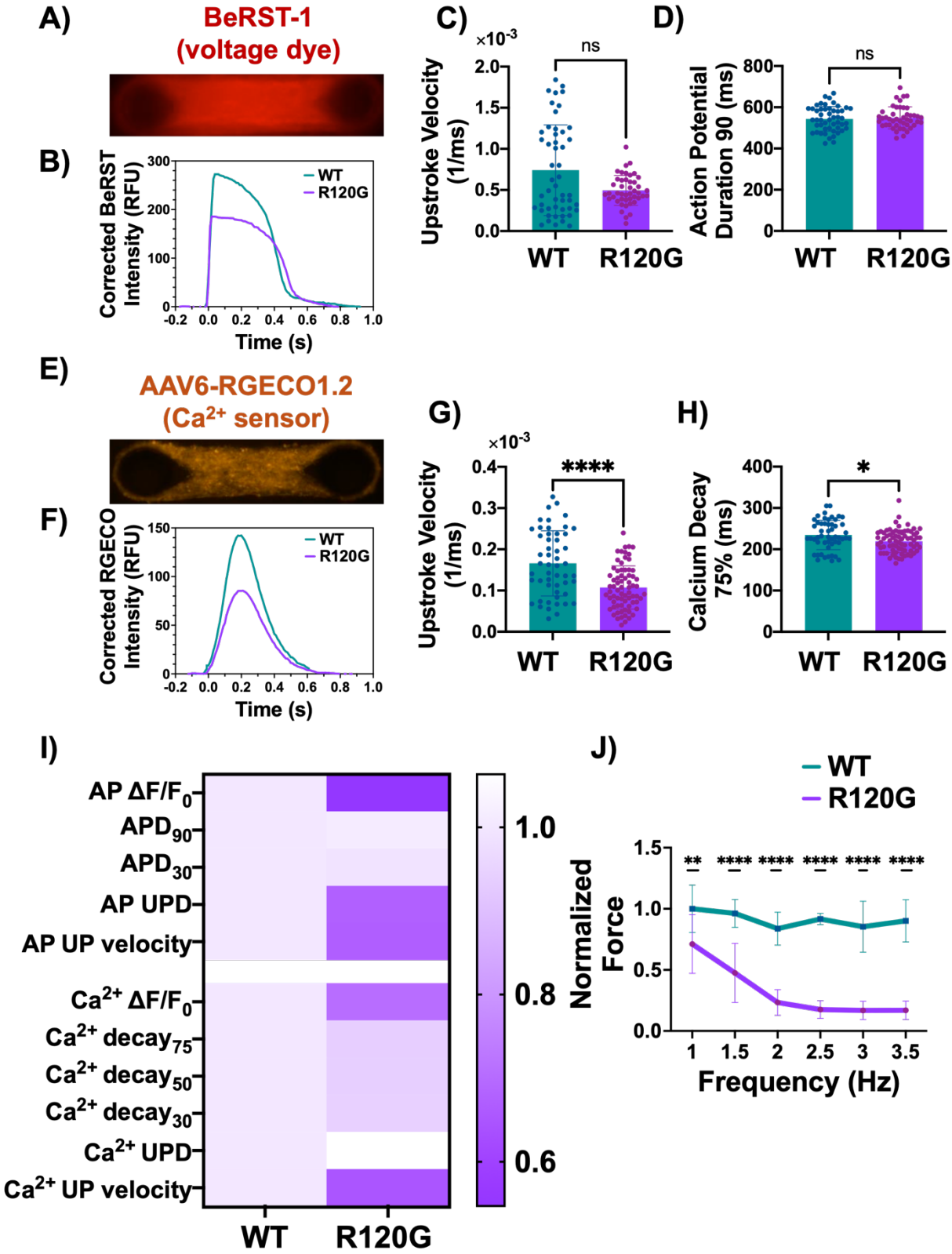
A)
BeRST-1
(voltage dye)
B)
Corrected BeRST Intensity (RFU)
Time (s)
WT
R120G
C)
Upstroke Velocity (1/ms)
ns
D)
Action Potential Duration 90 (ms)
ns
E)
AAV6-RGECO1.2
(Ca2+ sensor)
F)
Corrected RGECO Intensity (RFU)
Time (s)
G)
Upstroke Velocity (1/ms)
****
H)
Calcium Decay 75% (ms)
*
I)
AP ΔF/F0
APD90
APD30
AP UPD
AP UP velocity
Ca2+ ΔF/F0
Ca2+ decay75
Ca2+ decay50
Ca2+ decay30
Ca2+ UPD
Ca2+ UP velocity
J)
Normalized Force
Frequency (Hz)

787

788 **Figure 5. The CRYAB-R120G mutation impairs calcium handling in 3D µHTs. (A-**
789 **D)** Voltage measurements using BeRST-1 dye. **(A)** Representative image of µHT loaded with
790 BeRST-1 (voltage dye). **(B)** Representative corrected BeRST-1 intensity traces from CRYAB-WT
791 and CRYAB-R120G µHTs. Quantification of **(C)** upstroke velocity measured by normalized
792 background-corrected BeRST-1 signal intensity ($\Delta F/F_0$) over upstroke duration time and **(D)**
793 action potential duration at 90% repolarization (APD_{90}). CRYAB-R120G µHTs show significantly
794 reduced action potential amplitude with no significant change in APD_{90}. **(E-H)** Calcium
795 measurements using AAV6-RGECO1.2. **(E)** Representative image of µHT expressing RGECO1.2
796 (genetically encoded Ca^{2+} sensor). **(F)** Representative corrected RGECO1.2 intensity traces from
797 CRYAB-WT and CRYAB-R120G µHTs. Quantification of **(G)** upstroke velocity measured by
798 normalized background-corrected RGECO signal intensity ($\Delta F/F_0$) over upstroke duration time
799 and **(H)** Ca^{2+} decay time to 75% of peak. CRYAB-R120G µHTs show significantly reduced Ca^{2+}
800 transient amplitude and prolonged decay kinetics. **(I)** Heatmap of normalized electrophysiological
801 and Ca^{2+} handling parameters, including AP amplitude ($\Delta F/F_0$), APD_{90}, APD_{30}, AP upstroke
802 duration (AP UPD), AP upstroke velocity (AP UP velocity), Ca^{2+} amplitude ($\Delta F/F_0$), Ca^{2+} decay
803 times (75%, 50%, 30% of peak), Ca^{2+} UPD, and Ca^{2+} upstroke velocity (UP velocity). All values
804 are normalized to the mean WT values, with darker purple indicating lower relative values. Data
805 are presented as mean ± *SD*; n values represent individual µHT pooled from ≥3 independent
806 differentiations. *P* values by unpaired t-test for parametric data (APD_{90}) and Mann–Whitney test
807 for non-parametric data (BeRST upstroke velocity, RGECO upstroke velocity, and Ca^{2+} decay).
808 **** $p < 0.0001$, * $p < 0.05$, ns = not significant. **(J)** Normalized Force–frequency relationship in
809 CRYAB-WT and CRYAB-R120G µHTs paced from 1 to 3.5 Hz, showing a pronounced negative
810 force–frequency response in CRYAB-R120G µHTs. Values are normalized to the mean WT peak

active force at 1 Hz pacing. Data are presented as mean ± *SD*; n values represent individual μHT pooled from one differentiation. Data were analyzed by two-way ANOVA, followed by Holm–Šidák's multiple comparison test.

Figure 6

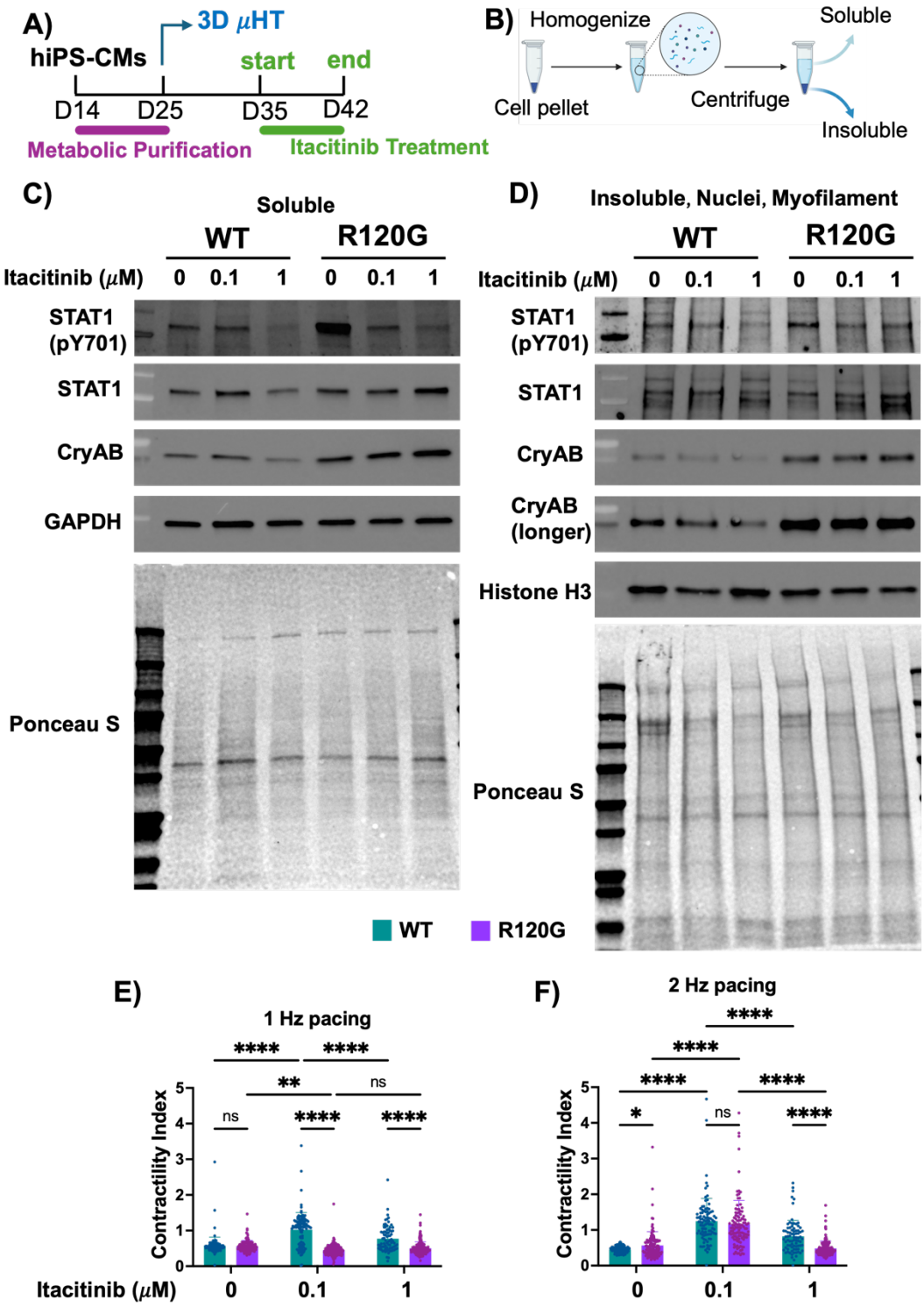

Figure 6. Itacitinib reduces STAT1 activation but does not fully rescue contractility deficit in CRYAB-R120G μHTs. (A) Schematic of the experimental timeline for treating μHTs with

817 Itacitinib. hiPS-CMs were metabolically purified (D14–D25) after differentiation, seeded into 3D
818 μHT devices (D25–D35), and treated with 0.1 and 1 μM Itacitinib and vehicle control from D35–
819 D42 before analysis. **(B)** μHTs were lysed using RIPA buffer with 1% NP-40 into soluble and
820 insoluble fractions. **(C)** Representative immunoblots of soluble fractions showing dose-dependent
821 reduction in phosphorylated STAT1 (pY701) in both CRYAB-WT and CRYAB-R120G μHTs
822 following treatment with 0.1 or 1 μM Itacitinib, with total STAT1 unchanged. Soluble CRYAB
823 levels were higher in CRYAB-R120G μHTs compared to CRYAB-WT across all conditions.
824 GAPDH was used as a loading control; Ponceau S staining shown as reference. **(D)** Representative
825 immunoblots of insoluble fraction containing aggregates/nuclear/myofilament fractions showing
826 dose-dependent reduction of phosphorylated STAT1 with Itacitinib treatment, while total STAT1
827 levels remained unchanged. CRYAB accumulated at higher levels in insoluble fractions of
828 CRYAB-R120G μHTs, regardless of treatment. Histone H3 was used as a loading control;
829 Ponceau S staining shown as reference. Blots are representative of 2 individual differentiation
830 batches. Contractility index (ratio of peak active force post-/pre-treatment at the same μHT) treated
831 with vehicle control, 0.1 μM, and 1 μM Itacitinib paced at **(E)** 1 Hz and **(F)** 2 Hz frequency. 0.1
832 μM Itacitinib partially rescued contractility at 2 Hz; however, 1 μM Itacitinib worsened
833 contractility. Data are presented as mean ± *SD*; n values represent individual μHTs pooled from
834 ≥2 independent differentiations.
835 Data were analyzed by two-way ANOVA, followed by Holm–Šidák's multiple comparison test.
836 **** $p < 0.0001$, *** $p < 0.001$, ** $p < 0.01$, ns = not significant.

References

1. Shahim B, Kapelios CJ, Savarese G, Lund LH. Global Public Health Burden of Heart Failure: An Updated Review. *Card Fail Rev*. 2023;9:e11.
2. Lakdawala NK, Stevenson LW, Loscalzo J. Cardiomyopathy and Myocarditis. In: Loscalzo J, Fauci A, Kasper D, Hauser S, Longo D, Jameson JL, editors. Harrison's Principles of Internal Medicine, 21e. New York, NY: McGraw-Hill Education; 2022.
3. Clemen CS, Herrmann H, Strelkov SV, Schröder R. Desminopathies: pathology and mechanisms. *Acta Neuropathologica*. 2013;125(1):47-75.
4. Muñoz-Mármol AM, Strasser G, Isamat M, Coulombe PA, Yang Y, Roca X, et al. A dysfunctional desmin mutation in a patient with severe generalized myopathy. *Proc Natl Acad Sci U S A*. 1998;95(19):11312-7.
5. Goldfarb LG, Park KY, Cervenáková L, Gorokhova S, Lee HS, Vasconcelos O, et al. Missense mutations in desmin associated with familial cardiac and skeletal myopathy. *Nat Genet*. 1998;19(4):402-3.
6. Vicart P, Caron A, Guicheney P, Li Z, Prévost MC, Faure A, et al. A missense mutation in the alphaB-crystallin chaperone gene causes a desmin-related myopathy. *Nat Genet*. 1998;20(1):92-5.
7. Goldfarb LG, Dalakas MC. Tragedy in a heartbeat: malfunctioning desmin causes skeletal and cardiac muscle disease. *The Journal of Clinical Investigation*. 2009;119(7):1806-13.
8. Marcos AT, Amorós D, Muñoz-Cabello B, Galán F, Rivas Infante E, Alcaraz-Mas L, et al. A novel dominant mutation in CRYAB gene leading to a severe phenotype with childhood onset. *Mol Genet Genomic Med*. 2020;8(8):e1290.
9. Islam M, Diwan, A., & Mani, K. . Come Together: Protein Assemblies, Aggregates and the Sarcostat at the Heart of Cardiac Myocyte Homeostasis. *Frontiers in Physiology*. 2020;11.
10. Martin TG, Myers VD, Dubey P, Dubey S, Perez E, Moravec CS, et al. Cardiomyocyte contractile impairment in heart failure results from reduced BAG3-mediated sarcomeric protein turnover. *Nature Communications*. 2021;12(1):2942.
11. Pohl C, Dikic I. Cellular quality control by the ubiquitin-proteasome system and autophagy. *Science*. 2019;366(6467):818-22.
12. Ranek MJ, Stachowski MJ, Kirk JA, Willis MS. The role of heat shock proteins and co-chaperones in heart failure. *Philos Trans R Soc Lond B Biol Sci*. 2018;373(1738).
13. Sciarretta S, Maejima Y, Zablocki D, Sadoshima J. The Role of Autophagy in the Heart. *Annu Rev Physiol*. 2018;80:1-26.
14. Kwon YT, Ciechanover A. The Ubiquitin Code in the Ubiquitin-Proteasome System and Autophagy. *Trends Biochem Sci*. 2017;42(11):873-86.
15. Diwadkar S, Patel AA, Fradley MG. Bortezomib-Induced Complete Heart Block and Myocardial Scar: The Potential Role of Cardiac Biomarkers in Monitoring Cardiotoxicity. *Case Reports in Cardiology*. 2016;2016(1):3456287.
16. Voortman J, Giaccone G. Severe reversible cardiac failure after bortezomib treatment combined with chemotherapy in a non-small cell lung cancer patient: a case report. *BMC Cancer*. 2006;6(1):129.
17. Gilda JE, Gomes AV. Proteasome dysfunction in cardiomyopathies. *J Physiol*. 2017;595(12):4051-71.

18. Ma X, Mani K, Liu H, Kovacs A, Murphy JT, Foroughi L, et al. Transcription Factor EB Activation Rescues Advanced αB-Crystallin Mutation-Induced Cardiomyopathy by Normalizing Desmin Localization. *J Am Heart Assoc*. 2019;8(4):e010866.
19. McLendon PM, Robbins J. Desmin-related cardiomyopathy: an unfolding story. *Am J Physiol Heart Circ Physiol*. 2011;301(4):H1220-8.
20. Singh SR, Kadioglu H, Patel K, Carrier L, Agnetti G. Is Desmin Propensity to Aggregate Part of its Protective Function? *Cells*. 2020;9(2).
21. Islam M, Rawnsley DR, Ma X, Navid W, Zhao C, Guan X, et al. Phosphorylation of CRYAB induces a condensatopathy to worsen post-myocardial infarction left ventricular remodeling. *J Clin Invest*. 2025;135(7).
22. Bennardini F, Wrzosek A, Chiesi M. Alpha B-crystallin in cardiac tissue. Association with actin and desmin filaments. *Circ Res*. 1992;71(2):288-94.
23. Darvazi M, Ghorbani M, Ramazi S, Allahverdi A, Abdolmaleki P. A computational study of the R120G mutation in human αB-crystallin: implications for structural stability and functionality. *Journal of Biomolecular Structure and Dynamics*. 2024;42(11):5788-98.
24. Clark AR, Naylor CE, Bagnéris C, Keep NH, Slingsby C. Crystal Structure of R120G Disease Mutant of Human αB-Crystallin Domain Dimer Shows Closure of a Groove. *Journal of Molecular Biology*. 2011;408(1):118-34.
25. Bova MP, Yaron O, Huang Q, Ding L, Haley DA, Stewart PL, et al. Mutation R120G in αB-crystallin, which is linked to a desmin-related myopathy, results in an irregular structure and defective chaperone-like function. *Proceedings of the National Academy of Sciences*. 1999;96(11):6137-42.
26. Sanbe A, Osinska H, Villa C, Gulick J, Klevitsky R, Glabe CG, et al. Reversal of amyloid-induced heart disease in desmin-related cardiomyopathy. *Proc Natl Acad Sci U S A*. 2005;102(38):13592-7.
27. Rajasekaran NS, Connell P, Christians ES, Yan LJ, Taylor RP, Orosz A, et al. Human alpha B-crystallin mutation causes oxido-reductive stress and protein aggregation cardiomyopathy in mice. *Cell*. 2007;130(3):427-39.
28. Wang X, Osinska H, Klevitsky R, Gerdes AM, Nieman M, Lorenz J, et al. Expression of R120G–αB-Crystallin Causes Aberrant Desmin and αB-Crystallin Aggregation and Cardiomyopathy in Mice. *Circulation Research*. 2001;89(1):84-91.
29. Pietsch N, Cheng J, Fazio A, Ewald L, Alizoti E, Krämer E, et al. Generation of a homozygous CRYAB p.Arg120Gly mutant (UKEi001-A-1) from a human iPSC line. *Stem Cell Research*. 2023;71:103188.
30. Welsh N, Margulis B, Borg LAH, Wiklund HJ, Saldeen J, Flodström M, et al. Differences in the Expression of Heat-Shock Proteins and Antioxidant Enzymes between Human and Rodent Pancreatic Islets: Implications for the Pathogenesis of Insulin-Dependent Diabetes Mellitus. *Molecular Medicine*. 1995;1(7):806-20.
31. Hashemi M, Finklea FB, Hammons H, Tian Y, Young N, Kim E, et al. Hydrogel microsphere stem cell encapsulation enhances cardiomyocyte differentiation and functionality in scalable suspension system. *Bioactive Materials*. 2025;43:423-40.
32. Feyen DAM, McKeithan WL, Bruyneel AAN, Spiering S, Hörmann L, Ulmer B, et al. Metabolic Maturation Media Improve Physiological Function of Human iPSC-Derived Cardiomyocytes. *Cell Reports*. 2020;32(3).

33. Tu C, Chao BS, Wu JC. Strategies for Improving the Maturity of Human Induced Pluripotent Stem Cell-Derived Cardiomyocytes. *Circulation Research*. 2018;123(5):512-4.
34. Lian X, Hsiao C, Wilson G, Zhu K, Hazeltine LB, Azarin SM, et al. Robust cardiomyocyte differentiation from human pluripotent stem cells via temporal modulation of canonical Wnt signaling. *Proceedings of the National Academy of Sciences*. 2012;109(27):E1848-E57.
35. Vermeer MCSC, Bolling MC, Bliley JM, Gomez KFA, Pavez-Giani MG, Kramer D, et al. Gain-of-function mutation in ubiquitin ligase KLHL24 causes desmin degradation and dilatation in hiPSC-derived engineered heart tissues. *The Journal of Clinical Investigation*. 2021;131(17).
36. Alisafaei F, Shakiba D, Hong Y, Ramahdita G, Huang Y, Iannucci LE, et al. Tension anisotropy drives fibroblast phenotypic transition by self-reinforcing cell–extracellular matrix mechanical feedback. *Nature Materials*. 2025;24(6):955-65.
37. Ewoldt JK, Wang MC, McLellan MA, Cloonan PE, Chopra A, Gorham J, et al. Hypertrophic cardiomyopathy–associated mutations drive stromal activation via EGFR-mediated paracrine signaling. *Science Advances*. 2024;10(42):eadi6927.
38. McLendon PM, Davis G, Gulick J, Singh SR, Xu N, Salomonis N, et al. An Unbiased High-Throughput Screen to Identify Novel Effectors That Impact on Cardiomyocyte Aggregate Levels. *Circulation Research*. 2017;121(6):604-16.
39. Lund LM, Kerr JP, Lupinetti J, Zhang Y, Russell MA, Bloch RJ, et al. Synemin isoforms differentially organize cell junctions and desmin filaments in neonatal cardiomyocytes. *The FASEB Journal*. 2012;26(1):137-48.
40. Kim H-D. Expression of intermediate filament desmin and vimentin in the human fetal heart. *The Anatomical Record*. 1996;246(2):271-8.
41. Huebsch N, Charrez B, Neiman G, Siemons B, Boggess SC, Wall S, et al. Metabolically driven maturation of human-induced-pluripotent-stem-cell-derived cardiac microtissues on microfluidic chips. *Nat Biomed Eng*. 2022;6(4):372-88.
42. Wickramasinghe NM, Sachs D, Shewale B, Gonzalez DM, Dhanan-Krishnan P, Torre D, et al. PPARdelta activation induces metabolic and contractile maturation of human pluripotent stem cell-derived cardiomyocytes. *Cell Stem Cell*. 2022;29(4):559-76.e7.
43. Pachitariu M, Stringer C. Cellpose 2.0: how to train your own model. *Nature Methods*. 2022;19(12):1634-41.
44. Ramahdita G, Peng X, Jafari M, Pobee C, Bhakta R, Zhang Z, et al. 3D-printing-assisted, microfabricated devices reveal hierarchical and temporal mechanosensing in high-density fibroblast culture. *bioRxiv*. 2025:2025.09.18.677242.
45. Kok RNU, Spoelstra WK, Betjes MA, van Zon JS, Tans SJ. Label-free cell imaging and tracking in 3D organoids. *Cell Reports Physical Science*. 2025;6(4).
46. van Nuland TFW, van Dommelen JAW, Geers MGD. An anisotropic Voronoi algorithm for generating polycrystalline microstructures with preferred growth directions. *Computational Materials Science*. 2021;186:109947.
47. Leonard A, Bertero A, Powers JD, Beussman KM, Bhandari S, Regnier M, et al. Afterload promotes maturation of human induced pluripotent stem cell derived cardiomyocytes in engineered heart tissues. *Journal of Molecular and Cellular Cardiology*. 2018;118:147-58.
48. Guo J, Jiang H, Schuftan D, Moreno JD, Ramahdita G, Aryan L, et al. Substrate mechanics unveil early structural and functional pathology in iPSC micro-tissue models of hypertrophic cardiomyopathy. *iScience*. 2024;27(6).

49. Schuftan D, Kooh YKG, Guo J, Sun Y, Aryan L, Stottlemire B, et al. Dynamic control of contractile resistance to iPSC-derived micro-heart muscle arrays. *Journal of Biomedical Materials Research Part A*. 2024;112(4):534-48.
50. Xiong Y, Li G. Correlation Characteristics Between Urban Fires and Urban Functional Spaces: A Study Based on Point of Interest Data and Ripley's K-Function. *ISPRS International Journal of Geo-Information*. 2025;14(2):45.
51. Voges HK, Foster SR, Reynolds L, Parker BL, Devilée L, Quaife-Ryan GA, et al. Vascular cells improve functionality of human cardiac organoids. *Cell Reports*. 2023;42(5).
52. Su H, Wang X. The ubiquitin-proteasome system in cardiac proteinopathy: a quality control perspective. *Cardiovascular Research*. 2009;85(2):253-62.
53. Pattison JS, Osinska H, Robbins J. Atg7 Induces Basal Autophagy and Rescues Autophagic Deficiency in CryABR120G Cardiomyocytes. *Circulation Research*. 2011;109(2):151-60.
54. Chen Q, Liu JB, Horak KM, Zheng H, Kumarapeli AR, Li J, et al. Intrasarcoplasmic amyloidosis impairs proteolytic function of proteasomes in cardiomyocytes by compromising substrate uptake. *Circ Res*. 2005;97(10):1018-26.
55. Ohiri JC, Dellefave-Castillo L, Tomar G, Wilsbacher L, Choudhury L, Barefield DY, et al. Reduction of Filamin C Results in Altered Proteostasis, Cardiomyopathy, and Arrhythmias. *Journal of the American Heart Association*. 2024;13(10):e030467.
56. Huang Y, Wang Z, Liu Y, Xiong H, Zhao Y, Wu L, et al. αB-Crystallin Interacts with Na_v1.5 and Regulates Ubiquitination and Internalization of Cell Surface Na_v1.5 *. *Journal of Biological Chemistry*. 2016;291(21):11030-41.
57. Bers DM. Cardiac excitation–contraction coupling. *Nature*. 2002;415(6868):198-205.
58. Bielawski KS, Leonard A, Bhandari S, Murry CE, Sniadecki NJ. Real-Time Force and Frequency Analysis of Engineered Human Heart Tissue Derived from Induced Pluripotent Stem Cells Using Magnetic Sensing. *Tissue Eng Part C Methods*. 2016;22(10):932-40.
59. Rupert CE, Kim TY, Choi B-R, Coulombe KLK. Human Cardiac Fibroblast Number and Activation State Modulate Electromechanical Function of hiPSC-Cardiomyocytes in Engineered Myocardium. *Stem Cells International*. 2020;2020(1):9363809.
60. Cai M, Pan B, Xiao P, Bouska M, Lewno MT, Xing Y, et al. Sustained but Decoyed Activation of the JAK1-STAT Pathway by Aberrant Protein Aggregation Exacerbates Proteotoxicity. *Circulation (New York, NY)*. 2024;150(16):1302-5.
61. Alizoti E, Michler L, Orthey E, Osinska H, Gulick J, Klampe B, et al. JAK1 Inhibitors reduce CRYAB^{R120G} aggregates in rat and human cardiomyocytes. *Journal of Molecular and Cellular Cardiology*. 2022;173:S95-S6.
62. Zhan R-Z, Rao L, Chen Z, Strash N, Bursac N. Loss of sarcomeric proteins via upregulation of JAK/STAT signaling underlies interferon-γ-induced contractile deficit in engineered human myocardium. *Acta Biomaterialia*. 2021;126:144-53.
63. Han J, Lin L, Fang Z, Xu D, Wang L, Ye B, et al. Cardiomyocyte-derived USP13 protects hearts from hypertrophy via deubiquitinating and stabilizing STAT1 in male mice. *Nature Communications*. 2025;16(1):5927.
64. Li Z, Mericskay M, Agbulut O, Butler-Browne G, Carlsson L, Thornell L-E, et al. Desmin Is Essential for the Tensile Strength and Integrity of Myofibrils but Not for Myogenic Commitment, Differentiation, and Fusion of Skeletal Muscle. *Journal of Cell Biology*. 1997;139(1):129-44.

1012 65. Paulin D, Li Z. Desmin: a major intermediate filament protein essential for the structural
1013 integrity and function of muscle. *Experimental Cell Research*. 2004;301(1):1-7.
1014 66. Wang X, Klevitsky R, Huang W, Glasford J, Li F, Robbins J. αB-Crystallin Modulates
1015 Protein Aggregation of Abnormal Desmin. *Circulation Research*. 2003;93(10):998-1005.
1016 67. Agnetti G, Herrmann H, Cohen S. New roles for desmin in the maintenance of muscle
1017 homeostasis. *The FEBS Journal*. 2022;289(10):2755-70.
1018 68. Elliott JL, Der Perng M, Prescott AR, Jansen KA, Koenderink GH, Quinlan RA. The
1019 specificity of the interaction between αB-crystallin and desmin filaments and its
1020 impact on filament aggregation and cell viability. *Philosophical Transactions of the Royal Society*
1021 *B: Biological Sciences*. 2013;368(1617):20120375.
1022 69. Sanbe A, Osinska H, Saffitz JE, Glabe CG, Kayed R, Maloyan A, et al. Desmin-related
1023 cardiomyopathy in transgenic mice: a cardiac amyloidosis. *Proc Natl Acad Sci U S A*.
1024 2004;101(27):10132-6.
1025 70. Rawnsley DR, Islam M, Zhao C, Kargar Gaz Kooh Y, Mendoza A, Navid H, et al.
1026 Mitophagy Facilitates Cytosolic Proteostasis to Preserve Cardiac Function. *bioRxiv*.
1027 2024:2024.11.24.624947.
1028 71. McLendon PM, Robbins J. Desmin-related cardiomyopathy: an unfolding story. *American*
1029 *Journal of Physiology-Heart and Circulatory Physiology*. 2011;301(4):H1220-H8.
1030 72. Reimann J, Kunz WS, Vielhaber S, Kappes-Horn K, Schröder R. Mitochondrial
1031 dysfunction in myofibrillar myopathy. *Neuropathol Appl Neurobiol*. 2003;29(1):45-51.
1032 73. Alam S, Abdullah CS, Aishwarya R, Morshed M, Nitu SS, Miriyala S, et al. Dysfunctional
1033 Mitochondrial Dynamic and Oxidative Phosphorylation Precedes Cardiac Dysfunction in R120G-
1034 αB-Crystallin-Induced Desmin-Related Cardiomyopathy. *Journal of the American Heart*
1035 *Association*. 2020;9(23):e017195.
1036 74. Espejo MS, Aiello I, Sepúlveda M, Vila Petroff MG, Aiello EA, De Giusti VC. The reduced
1037 myofilament responsiveness to calcium contributes to the negative force-frequency relationship in
1038 rat cardiomyocytes: role of reactive oxygen species and p-38 map kinase. *Pflugers Arch*.
1039 2017;469(12):1663-73.
1040 75. Jiao Q, Sanbe A, Zhang X, Liu J-P, Minamisawa S. αB-Crystallin R120G variant causes
1041 cardiac arrhythmias and alterations in the expression of Ca2+-handling proteins and endoplasmic
1042 reticulum stress in mice. *Clinical and Experimental Pharmacology and Physiology*.
1043 2014;41(8):589-99.
1044 76. Yoshida H. ER stress and diseases. *The FEBS Journal*. 2007;274(3):630-58.
1045 77. Alizoti E, Ewald L, Parretta S, Meyer-Jens M, Orthey E, Conze C, et al. Ruxolitinib clears
1046 CRYAB p.Arg120Gly aggregates through the ubiquitin-proteasome system. *bioRxiv*.
1047 2024:2024.10.11.615348.
1048 78. Yang Q, Ji H, Modarresi Chahardehi A. JAK/STAT pathway in myocardial infarction:
1049 Crossroads of immune signaling and cardiac remodeling. *Mol Immunol*. 2025;186:206-17.
1050 79. Kishore R, Verma SK. Roles of STATs signaling in cardiovascular diseases. *JAK-STAT*.
1051 2012;1(2):118-24.
1052 80. Mascareno E, El-Shafei M, Maulik N, Sato M, Guo Y, Das DK, et al. JAK/STAT Signaling
1053 Is Associated With Cardiac Dysfunction During Ischemia and Reperfusion. *Circulation*.
1054 2001;104(3):325-9.

81. Pan J, Fukuda K, Saito M, Matsuzaki J, Kodama H, Sano M, et al. Mechanical Stretch Activates the JAK/STAT Pathway in Rat Cardiomyocytes. *Circulation Research*. 1999;84(10):1127-36.
82. Ho BX, Yu H, Pang JKS, Hor J-H, Liew LC, Szyniarowski P, et al. Upregulation of the JAK-STAT pathway promotes maturation of human embryonic stem cell-derived cardiomyocytes. *Stem Cell Reports*. 2021;16(12):2928-41.
83. Pocock MW, Reid JD, Robinson HR, Charitakis N, Krycer JR, Foster SR, et al. Maturation of human cardiac organoids enables complex disease modeling and drug discovery. *Nature Cardiovascular Research*. 2025;4(7):821-40.
84. Soares CP, Midlej V, Oliveira MEWd, Benchimol M, Costa ML, Mermelstein C. 2D and 3D-Organized Cardiac Cells Shows Differences in Cellular Morphology, Adhesion Junctions, Presence of Myofibrils and Protein Expression. *PLOS ONE*. 2012;7(5):e38147.
85. Simmons DW, Malayath G, Schuftan DR, Guo J, Oguntuyo K, Ramahdita G, et al. Engineered tissue geometry and Plakophilin-2 regulate electrophysiology of human iPSC-derived cardiomyocytes. *APL Bioengineering*. 2024;8(1).
86. Juguilon C, Khosravi R, Radisic M, Wu JC. In Vitro Modeling of Interorgan Crosstalk: Multi-Organ-on-a-Chip for Studying Cardiovascular-Kidney-Metabolic Syndrome. *Circulation Research*. 2025;136(11):1476-93.
87. Goldfracht I, Efraim Y, Shinnawi R, Kovalev E, Huber I, Gepstein A, et al. Engineered heart tissue models from hiPSC-derived cardiomyocytes and cardiac ECM for disease modeling and drug testing applications. *Acta Biomaterialia*. 2019;92:145-59.
88. Block T, Creech J, da Rocha AM, Marinkovic M, Ponce-Balbuena D, Jiménez-Vázquez EN, et al. Human perinatal stem cell derived extracellular matrix enables rapid maturation of hiPSC-CM structural and functional phenotypes. *Scientific Reports*. 2020;10(1):19071.
89. Nanavati BN, Noordstra I, Lwin AKO, Brooks JW, Rae J, Parton RG, et al. The desmosome-intermediate filament system facilitates mechanotransduction at adherens junctions for epithelial homeostasis. *Current Biology*. 2024;34(17):4081-90.e5.
90. Boriek AM, Capetanaki Y, Hwang W, Officer T, Badshah M, Rodarte J, et al. Desmin integrates the three-dimensional mechanical properties of muscles. *American Journal of Physiology-Cell Physiology*. 2001;280(1):C46-C52.
91. Price AJ, Cost A-L, Ungewiß H, Waschke J, Dunn AR, Grashoff C. Mechanical loading of desmosomes depends on the magnitude and orientation of external stress. *Nature Communications*. 2018;9(1):5284.
92. McCain ML, Lee H, Aratyn-Schaus Y, Kléber AG, Parker KK. Cooperative coupling of cell-matrix and cell–cell adhesions in cardiac muscle. *Proceedings of the National Academy of Sciences*. 2012;109(25):9881-6.
93. Snider J, Kotlyar M, Saraon P, Yao Z, Jurisica I, Stagljar I. Fundamentals of protein interaction network mapping. *Mol Syst Biol*. 2015;11(12):848.
94. Dimitrakis P, Romay-Ogando MI, Timolati F, Suter TM, Zuppinger C. Effects of doxorubicin cancer therapy on autophagy and the ubiquitin-proteasome system in long-term cultured adult rat cardiomyocytes. *Cell Tissue Res*. 2012;350(2):361-72.
95. Judge LM, Perez-Bermejo JA, Truong A, Ribeiro AJS, Yoo JC, Jensen CL, et al. A BAG3 chaperone complex maintains cardiomyocyte function during proteotoxic stress. *JCI Insight*. 2017;2(14).

96. Ho DLL, Lee S, Du J, Weiss JD, Tam T, Sinha S, et al. Large-Scale Production of Wholly Cellular Bioinks via the Optimization of Human Induced Pluripotent Stem Cell Aggregate Culture in Automated Bioreactors. *Adv Healthc Mater*. 2022;11(24):e2201138.
97. Simmons DW, Schuftan DR, Ramahdita G, Huebsch N. Hydrogel-Assisted Double Molding Enables Rapid Replication of Stereolithographic 3D Prints for Engineered Tissue Design. *ACS Applied Materials & Interfaces*. 2023;15(21):25313-23.
98. Malayath G, Huebsch N. Rapid thermoforming of polycarbonate cell culture accessories from 3D printed molds. *bioRxiv*. 2025:2025.07.07.663502.
99. Kargar Gaz Kooh Y, Huebsch N. Bridging high resolution sub-cellular imaging with physiologically relevant engineered tissues. *Frontiers in Mechanical Engineering*. 2024;Volume 10 - 2024.
100. Wu J, Liu L, Matsuda T, Zhao Y, Rebane A, Drobizhev M, et al. Improved orange and red $Ca^{2\pm}$ indicators and photophysical considerations for optogenetic applications. *ACS Chem Neurosci*. 2013;4(6):963-72.
101. Kim Y, Wang K, Lock RI, Nash TR, Fleischer S, Wang BZ, et al. BeatProfiler: Multimodal In Vitro Analysis of Cardiac Function Enables Machine Learning Classification of Diseases and Drugs. *IEEE Open Journal of Engineering in Medicine and Biology*. 2024;5:238-49.
102. Oguntuyo K, Schuftan D, Guo J, Simmons D, Bhagavan D, Moreno JD, et al. Robust, Automated Analysis of Electrophysiology in Induced Pluripotent Stem Cell-Derived Micro-Heart Muscle for Drug Toxicity. *Tissue Eng Part C Methods*. 2022;28(9):457-68.